The Astrophysical Journal, 790:127 (21pp), 2014 August 1 doi:10.1088/0004-637X/790/2/127

THE APOGEE RED-CLUMP CATALOG: PRECISE DISTANCES, VELOCITIES, AND HIGH-RESOLUTION ELEMENTAL ABUNDANCES OVER A LARGE AREA OF THE MILKY WAY'S DISK

Jo Bovy[1,39], David L. Nidever[2], Hans-Walter Rix[3], Léo Girardi[4,5], Gail Zasowski[6], S. Drew Chojnowski[7], Jon Holtzman[8], Courtney Epstein[9], Peter M. Frinchaboy[10], Michael R. Hayden[8], Thaíse S. Rodrigues[4,5], Steven R. Majewski[7], Jennifer A. Johnson[9,11], Marc H. Pinsonneault[9], Dennis Stello[12,13], Carlos Allende Prieto[14,15], Brett Andrews[9], Sarbani Basu[16], Timothy C. Beers[17,18], Dmitry Bizyaev[19], Adam Burton[7], William J. Chaplin[13,20], Katia Cunha[21,22], Yvonne Elsworth[13,20], Rafael A. García[23], Domingo A. García-Hernández[14,15], Ana E. García Pérez[7], Fred R. Hearty[24], Saskia Hekker[25], Thomas Kallinger[26], Karen Kinemuchi[19], Lars Koesterke[27], Szabolcs Mészáros[28], Benoît Mosser[29], Robert W. O'Connell[7], Daniel Oravetz[19], Kaike Pan[19], Annie C. Robin[30], Ricardo P. Schiavon[31], Donald P. Schneider[24,32], Mathias Schultheis[33], Aldo Serenelli[34], Matthew Shetrone[35], Victor Silva Aguirre[13], Audrey Simmons[19], Michael Skrutskie[7], Verne V. Smith[21,36], Keivan Stassun[37,38], David H. Weinberg[9,11], John C. Wilson[7], and Olga Zamora[14,15]

[1] Institute for Advanced Study, Einstein Drive, Princeton, NJ 08540, USA; bovy@ias.edu
[2] Department of Astronomy, University of Michigan, Ann Arbor, MI 48109, USA
[3] Max-Planck-Institut für Astronomie, Königstuhl 17, D-69117 Heidelberg, Germany
[4] Osservatorio Astronomico di Padova-INAF, Vicolo dell'Osservatorio 5, I-35122 Padova, Italy
[5] Laboratório Interinstitucional de e-Astronomia-LIneA, Rua Gal. José Cristino 77, Rio de Janeiro, RJ-20921-400, Brazil
[6] Department of Physics and Astronomy, Johns Hopkins University, Baltimore, MD 21218, USA
[7] Department of Astronomy, University of Virginia, Charlottesville, VA, 22904, USA
[8] New Mexico State University, Las Cruces, NM 88003, USA
[9] Department of Astronomy, The Ohio State University, Columbus, OH 43210, USA
[10] Department of Physics and Astronomy, Texas Christian University, Fort Worth, TX 76129, USA
[11] Center for Cosmology and Astro-Particle Physics, The Ohio State University, Columbus, OH 43210, USA
[12] Sydney Institute for Astronomy (SIfA), School of Physics, University of Sydney, NSW 2006, Australia
[13] Stellar Astrophysics Centre, Department of Physics and Astronomy, Aarhus University, DK-8000 Aarhus C, Denmark
[14] Instituto de Astrofísica de Canarias (IAC), E-38200 La Laguna, Tenerife, Spain
[15] Departamento de Astrofísica, Universidad de La Laguna (ULL), E-38206 La Laguna, Tenerife, Spain
[16] Department of Astronomy, Yale University, P.O. Box 208101, New Haven, CT 06520-8101, USA
[17] National Optical Astronomy Observatory, Tucson, AZ 85719, USA
[18] JINA: Joint Institute for Nuclear Astrophysics, Michigan State University, East Lansing, MI, USA
[19] Apache Point Observatory and New Mexico State University, P.O. Box 59, Sunspot, NM, 88349-0059, USA
[20] University of Birmingham, School of Physics and Astronomy, Edgbaston, Birmingham B15 2TT, UK
[21] Observatório Nacional, Rio de Janeiro, RJ 20921-400, Brazil
[22] Steward Observatory, U. Arizona, Tucson, AZ 85719, USA
[23] Laboratoire AIM, CEA/DSM-CNRS-Universite Paris Diderot, IRFU/SAp, Centre de Saclay, F-91191 Gif-sur-Yvette Cedex, France
[24] Department of Astronomy & Astrophysics, The Pennsylvania State University, 525 Davey Laboratory, University Park PA 16802, USA
[25] Max-Planck-Institut für Sonnensystemforschung, Justus-von-Liebig-Weg 3, D-37077 Göttingen, Germany
[26] Institute for Astronomy, University of Vienna, Turkenschanzstrasse 17, A-1180 Vienna, Austria
[27] Texas Advanced Computing Center, University of Texas, Austin, TX 78759, USA
[28] Department of Astronomy, Indiana University, Bloomington, IN 47405-7105, USA
[29] LESIA, CNRS, Université Pierre et Marie Curie, Université Denis Diderot, Observatoire de Paris, F-92195 Meudon, France
[30] Institute Utinam, CNRS UMR6213, Université de Franche-Comté, OSU THETA de Franche-Comté-Bourgogne, Besancon, France
[31] Astrophysics Research Institute, IC2, Liverpool Science Park, Liverpool John Moores University, 146 Brownlow Hill, Liverpool, L3 5RF, UK
[32] Institute for Gravitation and the Cosmos, The Pennsylvania State University, University Park, PA 16802, USA
[33] Laboratoire Lagrange (UMR7293), Université de Nice Sophia Antipolis, CNRS, Observatoire de la Côte d'Azur, BP 4229, F-06304 Nice Cedex 4, France
[34] Institute of Space Sciences (CSIC-IEEC), Campus UAB, Bellaterra, E-08193, Spain
[35] The University of Texas at Austin, McDonald Observatory, TX 79734, USA
[36] National Optical Astronomy Observatory, Tucson, AZ 85719, USA
[37] Physics and Astronomy Department, Vanderbilt University, 1807 Station B, Nashville, TN 37235, USA
[38] Department of Physics, Fisk University, 1000 17th Avenue North, Nashville, TN 37208, USA
Received 2014 March 28; accepted 2014 June 9; published 2014 July 14

ABSTRACT

The Sloan Digital Sky Survey III's Apache Point Observatory Galactic Evolution Experiment (APOGEE) is a high-resolution near-infrared spectroscopic survey covering all of the major components of the Galaxy, including the dust-obscured regions of the inner Milky Way disk and bulge. Here we present a sample of 10,341 likely red-clump stars (RC) from the first two years of APOGEE operations, selected based on their position in color–metallicity–surface-gravity–effective-temperature space using a new method calibrated using stellar evolution models and high-quality asteroseismology data. The narrowness of the RC locus in color–metallicity–luminosity space allows us to assign distances to the stars with an accuracy of 5%–10%. The sample extends to typical distances of about 3 kpc from the Sun, with some stars out to 8 kpc, and spans a volume of approximately 100 kpc^3 over 5 kpc $\lesssim R \lesssim$ 14 kpc, $|Z| \lesssim 2$ kpc, and $-15^\circ \lesssim$ Galactocentric azimuth $\lesssim 30^\circ$. The APOGEE red-clump (APOGEE-RC) catalog contains photometry from the Two Micron All Sky Survey, reddening estimates, distances, line-of-sight velocities, stellar parameters and elemental abundances determined from the high-resolution APOGEE spectra, and matches to major proper motion catalogs. We determine the survey selection function for this data set and discuss how the RC selection samples the underlying stellar populations. We use this sample to limit any

azimuthal variations in the median metallicity within the $\approx 45^\circ$ azimuthal region covered by the current sample to be $\leqslant 0.02$ dex, which is more than an order of magnitude smaller than the radial metallicity gradient. This result constrains coherent non-axisymmetric flows within a few kiloparsecs from the Sun.

Key words: Galaxy: abundances – Galaxy: disk – Galaxy: stellar content – Galaxy: structure – stars: distances – stars: general

Online-only material: color figures

1. INTRODUCTION

The Milky Way (MW) as a galaxy constitutes a unique laboratory for galaxy formation and evolution studies because, unlike for external galaxies, we can determine the high-dimensional stellar distribution of positions, velocities, ages, elemental abundances, etc., in detail using observations of individual stars (e.g., Rix & Bovy 2013). Unraveling the history of the MW in large part amounts to understanding the multifarious correlations among these observables, the question of distinct or smoothly blended sub-components, and variations in this distribution, and deducing its co-evolution with the other major components of the Galaxy—gas and dark matter—over the course of cosmic history.

Elemental abundances and their correlation with the spatial distribution and kinematics of stars are key to improving our knowledge of the chemo-dynamical structure of the MW (e.g., Bovy et al. 2012c, 2012d). As detailed elemental abundance patterns cannot be derived from broadband photometry, spectroscopic surveys are and will remain a necessary complement to large-area photometric and astrometric surveys (e.g., Pan-STARRS, Kaiser et al. 2002; SkyMapper, Keller et al. 2007; *Gaia*, de Bruijne 2012). Using current measurements of the distribution of stellar mass (Bovy & Rix 2013), 80% of the stars in the MW disk lie at $R < R_0$ and $|Z| < 1$ kpc, where R_0 is the distance from the Sun to the Galactic center and R and Z are Galactocentric cylindrical coordinates. Much of this volume is heavily extincted by dust obscuration and therefore difficult to access using optical spectroscopic surveys or *Gaia*. SDSS-III's APOGEE (Eisenstein et al. 2011; S. R. Majewski et al., in preparation) is a high-resolution spectroscopic survey that circumvents this difficulty by operating in the near-infrared ($\approx 1.6\,\mu$m) where extinction by dust is almost an order of magnitude smaller than at visible wavelengths.

In order to obtain high-resolution spectra in the infrared for stars out to large distances in the disk, APOGEE is primarily a survey of bright giants, for which distances are typically quite imprecise ($\gtrsim$20% uncertainty; e.g., Binney et al. 2014, Santiago et al. 2014, M. Hayden et al., in preparation). This makes it difficult to study the fine-grained distribution of velocities and elemental abundances as a function of location in the disk, because at several kiloparsecs, distance uncertainties are comparable to the scale over which significant gradients in kinematics (H I streaming motions over $\approx$1 kpc; e.g., Levine et al. 2008), metallicity (≈ -0.1 dex kpc^{-1} near the plane; e.g., Anders et al. 2014; Hayden et al. 2014; see also Section 7), or level of alpha-enhancement exist (e.g., Bovy et al. 2012d). In this paper, we identify a sample of red-clump star (RC) candidates in the APOGEE data for which the narrow distribution in the color–magnitude space allows assignment of distances that are accurate to about 5%–10%, which is smaller than the scale over which significant Galactic gradients exist even at the largest distances in our sample.

[39] Hubble fellow.

The RC is a prominent feature in the color–magnitude diagram (CMD) of stars that corresponds to the core-helium-burning stage in stellar evolution of low-mass stars. Because the luminosity distribution of the RC is very narrow, with a peak magnitude that does not depend very strongly on age or metallicity (see below), the magnitude of the RC has been widely used as a distance indicator (Paczynski & Stanek 1998). Through isolating the RC in the CMD and calibrating its luminosity using local data from *Hipparcos* (ESA 1997), precise distances to the Galactic center (Paczynski & Stanek 1998), various parts of the Galactic bulge (McWilliam & Zoccali 2010; Nataf et al. 2010), the Large Magellanic Cloud (Stanek et al. 1998; Udalski et al. 1998), M31 (Stanek & Garnavich 1998), and many other external galaxies (e.g., Girardi & Salaris 2001) have been obtained. This method relies on finding the RC based on its color, and the fact that it represents a significant overdensity in the CMD of a sample of stars at approximately a single distance.

Here we identify individual RC candidates in order to obtain distances to individual stars. These stars are not at a single distance, and therefore they cannot be isolated by searching for an overdensity in the observed CMD. Thus, we require a more detailed understanding of the RC to select likely RC stars for which we can obtain precise distances, based on the stars' atmospheric parameters and colors. In previous studies, the RC method for individual stars has assumed that the RC has a mean magnitude that does not depend on color or metallicity, and that the color of the RC is not strongly affected by metallicity (e.g., Siebert et al. 2011; Williams et al. 2013). It is clear, however, from theoretical isochrones produced by various stellar evolution codes (e.g., Girardi & Salaris 2001) that these assumptions are not valid, especially the latter, and applying a metallicity-independent color selection of RC stars will result in strong contamination ($\gtrsim$30%) from red-giant stars that are at quite different distances (up to 1 mag in distance modulus; see Section 2).

The APOGEE-RC sample presented in this paper corresponds to two years of APOGEE data and contains 10,341 stars over a volume of about 100 kpc^3 that approximately spans 5 kpc $\lesssim R \lesssim$ 14 kpc, $|Z| \lesssim$ 2 kpc, and $-15^\circ \lesssim$ Galactocentric azimuth $\lesssim 30^\circ$. Most stars in the current sample lie within 5 kpc from the Sun. As APOGEE continues acquiring data, longer integrations designed to reach fainter stars will extend the reach to $\approx$10 kpc toward the outer Galaxy, where extinction is low, and to $\approx$8 kpc toward the inner MW. SDSS-IV's APOGEE-2 (Sobeck et al. 2014), a continuation of the APOGEE survey starting in 2014 July, of which a major component is a similar survey conducted from the southern hemisphere, will extend the coverage of this red-clump sample to full 360° coverage of the Galactic plane with an additional 10,000+ sample of stars. The APOGEE-RC catalog will be publicly released with SDSS-III's Data Release 11/12 in 2014 December (see Section 6). We are presenting this description of the catalog now because the sample forms the basis of forthcoming science papers and such that the community can anticipate its availability.

A brief outline of this paper is as follows. We describe our new method for selecting RC stars from near-infrared photometry

and high-resolution spectroscopic data in Section 2. In Section 3, we describe our calibration of the RC distance scale for our sample using local *Hipparcos* data. We present the sample selection function for the APOGEE sample in Section 4 and determine the manner in which our RC selection samples the underlying Galactic stellar populations in Section 5. We provide a description of the RC catalog in Section 6. In Section 7, we investigate radial and azimuthal gradients in the metallicity distribution near the MW's midplane using the APOGEE-RC sample, allowing us to limit the ellipticity of the MW disk and constrain significant redistribution of angular momentum on kiloparsec scales over the last Gyr. Section 8 concludes the paper.

In this study, we transform distances and velocities to the left-handed Galactocentric rest-frame by assuming that the Sun's displacement from the midplane is 25 pc toward the north Galactic pole (Chen et al. 2001; Jurić et al. 2008) and that the Sun is located at 8 kpc from the Galactic center (e.g., Ghez et al. 2008; Gillessen et al. 2009; Bovy et al. 2009).

2. SELECTION OF A PURE RED-CLUMP SAMPLE IN APOGEE

2.1. APOGEE Observations and Data

The APOGEE is a near-infrared (NIR; H-band; 1.51 to 1.70 μm), high-resolution ($R \approx 22{,}500$), spectroscopic survey. The APOGEE instrument (Wilson et al. 2010; J. Wilson et al., in preparation) consists of a spectrograph with 300 2″ fibers that reaches a signal-to-noise ratio of 100 per half-resolution element (≈141 per resolution element) at $H \leqslant 12.2$ in three ≈one-hour visits during bright time on the 2.5 m Sloan telescope, located at the Apache Point Observatory in Sunspot, NM (Gunn et al. 2006). A detailed description of the target selection and data reduction pipeline is presented in Zasowski et al. (2013) and D. Nidever et al. (in preparation), respectively.

The photometry for all APOGEE targets is corrected for extinction with the Rayleigh Jeans Color Excess method (RJCE; Majewski et al. 2011). This technique provides extinction values A_{K_s} by making use of the near constancy of the near-to-mid-infrared $(H - [4.5\,\mu])_0$ color and calculating A_{K_s} as

$$A_{K_s} = 0.918\,(H - [4.5\,\mu] - 0.08), \quad (1)$$

where $H - [4.5\,\mu]$ is the measured color. NIR photometry comes from the Two Micron All Sky Survey (2MASS) catalog (Skrutskie et al. 2006) and mid-IR (MIR) photometry is obtained from *Spitzer*/IRAC GLIMPSE-I, -II, and -3D (Churchwell et al. 2009) when available and from WISE (Wright et al. 2010) otherwise. Typical photometric uncertainties for the stars in the RC catalog defined below are ∼0.02 mag in (J, H, K_s) and ∼0.05 mag in [4.5 μ], increasing to ∼0.03 mag and ∼0.10 mag in NIR and MIR photometry, respectively, at the faintest end of the APOGEE catalog ($H \sim 13.8$). The intrinsic color spread in $(H - [4.5\,\mu])_0$ is ∼0.01 mag for evolved stars with $0.5 \lesssim (J - K_s)_0) \lesssim 0.8$ (Majewski et al. 2011). Therefore, typical random uncertainties in the A_{K_s} extinction corrections are ∼0.05 mag, increasing to ∼0.10 mag at the faint end. Variations in the adopted extinction law among different lines of sight can lead to systematic uncertainties of up to 3.5% in A_{K_s} (Zasowski et al. 2009), which are typically 0.005 mag and <0.023 mag for all but 1% of our RC sample below. The contribution from the uncertainty in the extinction correction therefore plays only a minor role in the error budget of the RC distances that we determine below.

For each individual visit, line-of-sight velocities are measured separately by cross-correlating against a set of ≈100 synthetic template spectra that span the stellar-parameter range 3500 K < $T_{\rm eff}$ < 25,000 K in effective temperature $T_{\rm eff}$, −2 < [Fe/H] < 0.3 in metallicity [Fe/H], and 2 < log g < 5 in surface gravity log g (see D. Nidever et al. 2014a, in preparation, for further details; the reduction pipeline was also briefly described in Nidever et al. 2012). The rms scatter in the measured line-of-sight velocity for multiply observed stars is typically 0.1 km s^{-1}. Field-to-field variations indicate that the zero point of the velocity scale is stable at the 0.13 km s^{-1} level. A comparison between the APOGEE-measured line-of-sight velocity of 195 stars with literature data in the globular clusters M3, M13, M15, and M92 shows that the APOGEE zeropoint accuracy is ≈−0.95 ± 0.05 km s^{-1}.

The APOGEE Stellar Parameter and Chemical Abundances Pipeline (ASPCAP) extracts stellar parameters and elemental abundances from the continuum normalized co-added spectra by performing a χ^2 minimization with respect to a pre-computed multi-dimensional grid of synthetic spectra derived from ATLAS9 model-atmosphere grids (Kurucz 1979 and more recent updates) and spectral synthesis calculations using ASSϵT (Koesterke et al. 2008; Koesterke 2009); ASPCAP is described in detail in A. E. García Pérez (in preparation). The products of this procedure are best-fitting effective temperatures $T_{\rm eff}$, surface gravities log g, metallicities [Fe/H], α- [α/Fe], carbon- [C/Fe], and nitrogen-enhancements [N/Fe]. We find that the differences with spherical MARCS (Gustafsson et al. 2008)/Turbospectrum (Alvarez & Plez 1998; Plez 2012) spectra are below 5% for the atmospheric parameters typical of RC stars. Systematic offsets between the ASPCAP results and literature values for stellar parameters in open and globular clusters, as well as for seismic log g derived from asteroseismology of *Kepler* stars observed by APOGEE, were quantified by Mészáros et al. (2013). For the purpose of this paper, we use the corrected stellar parameters and abundances as determined from this external comparison. Because the ASPCAP fit metallicity was primarily calibrated against [Fe/H] from high-resolution optical spectroscopy, we refer to the metallicity as [Fe/H]. ASPCAP uncertainties are typically 50 to 100 K in $T_{\rm eff}$, 0.2 dex in log g, and 0.03 to 0.08 dex in [Fe/H] (Mészáros et al. 2013). For identifying a pure sample of RC stars using the method described below, log g in particular is crucial. Using the APOKASC asteroseismology data described in more detail below, we empirically determine the uncertainty in the spectroscopic log g to be 0.14 dex for APOGEE stars with $0.5 \lesssim (J - K_s)_0 \lesssim 0.8$ by comparison with the highly accurate seismic log g. As discussed in more detail in Section 2.3, part of this uncertainty is due to a relative bias in log g between the RC and the red-giant branch (RGB); when this bias will be removed, we estimate from the seismic log g that the spectroscopic log g uncertainty will be 0.1 dex. In addition to the main atmospheric parameters, the current ASPCAP pipeline is able to determine elemental abundances for 15 individual elements. However, the reliability of these still requires more testing.

2.2. RC Selection and Distance Determination

In this section, we describe a new method for selecting a sample of likely red-clump giants from a combination of photometric and spectroscopic data. This method is developed using isochrone models calculated by stellar evolution codes,

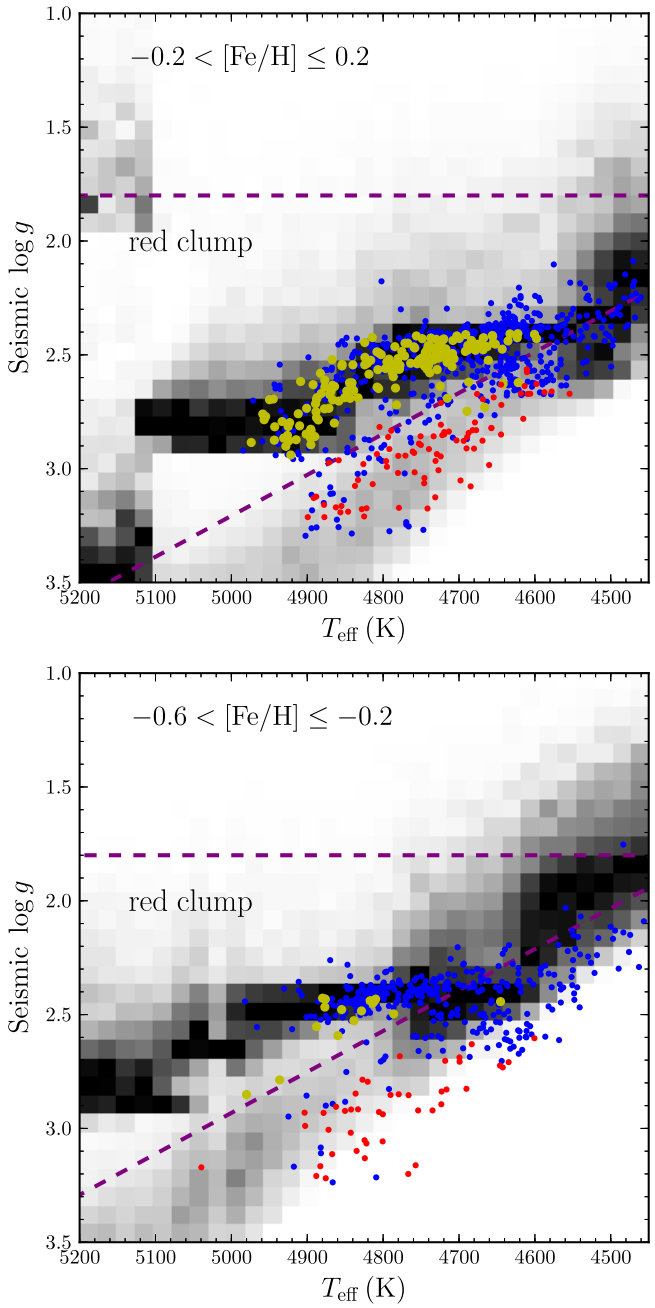

Figure 1. Prediction for the conditional distribution of stars in surface gravity given their effective temperature from the PARSEC stellar isochrones (see the text; density grayscale) and data from the APOKASC catalog (colored points), in two metallicity bins. The prediction assumes a lognormal Chabrier (2001) model for the IMF, a metallicity distribution that matches that of the APOKASC data used in each bin, and a constant SFH. The agreement between the models and the data is excellent in the region of the red clump. Yellow and red points represent stars classified by Stello et al. (2013) as RC and RGB stars, respectively, from their measured oscillation frequencies; blue points are stars for which the evolutionary state is unknown. The purple dashed lines represent our cuts in $\log g$ and $T_{\rm eff}$ to separate RC stars from less luminous red giant branch stars (see Equations (2) and (3); evaluated at [Fe/H] = 0 dex and [Fe/H] = −0.4 dex in the top and bottom panel, respectively). Additional cuts in $(J-K_s)_0$ and metallicity are used to reduce contamination from higher luminosity giants and secondary red-clump stars.

(A color version of this figure is available in the online journal.)

primarily from the PARSEC library (Bressan et al. 2012). To test whether these isochrone models are in agreement with the parameters inferred from APOGEE spectra, we use data from the APOKASC catalog (M. Pinsonneault et al., in preparation). This catalog contains stars in the *Kepler* field which have stellar parameters (mass, radius, and $\log g$) determined from asteroseismology (e.g., Kallinger et al. 2010) and $T_{\rm eff}$ and elemental abundances determined by APOGEE. The APOKASC asteroseismic analysis uses spectroscopic $T_{\rm eff}$ from APOGEE rather than $T_{\rm eff}$ from the Kepler Input Catalog (Brown et al. 2011). The combination of $\log g$ accurate to a few percent (Hekker et al. 2013) and metallicity measurements allows for a stringent test of the stellar isochrone models used here to define a red clump sample.

Figure 1 compares the prediction from the PARSEC stellar isochrones for the distribution of stars in effective temperature $T_{\rm eff}$ and surface-gravity $\log g$ with the data in the APOKASC catalog, in two different metallicity bins. The predicted distribution assumes a lognormal Chabrier (2001) model for the initial mass function (IMF) and a metallicity distribution that matches that of the APOKASC data used in each bin. For the distribution of ages we assume a constant star-formation history (SFH); throughout this paper we only use ages less than 10 Gyr. This assumption does not strongly affect the locus of the RC and the RGB in the $\log g$–$T_{\rm eff}$ diagram. Figure 1 shows excellent agreement between the predictions from the stellar evolution models and the data in the region of the red clump. Yellow and red points in the figure are stars in the APOKASC catalog for which the evolutionary state was measured by Stello et al. (2013) using the period spacings of gravity-mode stellar oscillations derived with two different methods (Bedding et al. 2011; Mosser et al. 2011). Yellow dots are stars classified as RC stars, while red dots represent stars identified as RGB stars. In the $\log g$–$T_{\rm eff}$ plane, the PARSEC isochrone models match the observed locus of RC and RGB stars, especially around solar metallicity. We have also compared the stellar-evolution models with the high-resolution spectroscopic $T_{\rm eff}$ and $\log g$ of the RC sample of Valentini & Munari (2010) and find similarly good agreement.

Motivated by the good agreement between the stellar isochrones and the APOKASC data, we use the theoretical models to investigate the morphology of the RC, such that we can determine the range of observed quantities for which the RC is sufficiently narrow in absolute magnitude to allow for a precise distance measurement for individual stars. In addition to the PARSEC models, we use various other stellar isochrone libraries to determine the theoretical uncertainty in the models; comparisons with these alternative libraries are described in detail below. Figure 1 demonstrates that red-clump stars have $\log g$ between 2.4 and 2.9 and are comfortably separated in $\log g$ and $T_{\rm eff}$ from the other main features in the CMD for stars with precise $\log g$ measurements. At high $\log g$, we adopt a sloping cut in $\log g$ as a function of $T_{\rm eff}$ to separate the RC and RGB branches. From the PARSEC isochrone models, we find that the slope separating the RC and the RGB does not vary with metallicity, but the intercept does. We will therefore select red-clump stars starting with the cuts

$$1.8 \leqslant \log g \leqslant 0.0018 \text{ dex K}^{-1} \left(T_{\rm eff} - T_{\rm eff}^{\rm ref}([\text{Fe/H}])\right) + 2.5, \quad (2)$$

where

$$T_{\rm eff}^{\rm ref}([\text{Fe/H}]) = -382.5 \text{ K dex}^{-1} [\text{Fe/H}] + 4607 \text{ K}. \quad (3)$$

It can be seen in Figure 1 that most of the solar-metallicity RC is at $\log g = 2.5$ and $4600 \text{ K} < T_{\rm eff} < 4850 \text{ K}$, but there is also a significant tail of such stars extending up to $T_{\rm eff} = 4950$ K and with $\log g$ increasing up to 2.9. These are the secondary red-clump stars, i.e., higher-mass helium-burning stars

(Girardi 1999), which are slightly overrepresented in the APOKASC sample (see M. Pinnsoneault et al., in preparation). These stars pass the cuts specified in Equations (2) and (3), even though they are expected to be significantly fainter than the main red clump (i.e., those RC stars at $\log g = 2.5$).

To further remove contamination from lower $\log g$ RGB and secondary red-clump stars, and to isolate RC stars for which precise distances can be derived, we further investigate the color–magnitude–metallicity distribution. We use the dereddened $(J - K_s)_0$ color rather than $T_{\rm eff}$, because of concerns about systematic biases in the latter in the measurement and in the stellar models. The $(J - K_s)_0$ color is sensitive to errors in the dereddening, but from the discussion in Section 2.1, it is clear that these are primarily random errors. Because the RC dominates the star counts at apparent magnitudes probed by APOGEE in the range $0.5 \lesssim (J - K_s)_0 \lesssim 0.8$ and because the RC luminosity is only a weak function of color (see below), random dereddening errors do no lead to significant contamination or distance errors.

We construct a model for the color–magnitude distribution (CMD) $(J - K_s)_0$ vs. M_{K_s} for RC-like stars in the PARSEC isochrones for a given metallicity Z; to increase the theoretical sampling, we average the isochrones for metallicities Z, $Z - 0.0005$, and $Z + 0.0005$. We apply the above cut in $\log g$, $T_{\rm eff}$, and [Fe/H] to the isochrones, which are sampled at equally spaced initial masses. We then create a density model by applying a kernel-density estimation (KDE) technique with a spherical kernel (after normalizing the color and magnitude by their standard deviations σ_{J-K_s}[40] and σ_{K_s}, respectively) that varies with position to account for the strongly varying density in the color–magnitude plane (Silverman 1986). Thus, the density at a point $\mathbf{x} \equiv ((J - K_s/\sigma_{J-K_s}), (M_{K_s}/\sigma_{K_s}))$ is evaluated as

$$p(\mathbf{x}) \propto \sum_i \frac{w_i}{\lambda_i^2} K\left(\frac{\mathbf{x} - \mathbf{x}_i}{h\,\lambda_i}\right), \tag{4}$$

where i indexes points $\mathbf{x}_i$ on the isochrones, and $K(\cdot)$ is the biweight kernel $K(\mathbf{r}) \propto (1 - r^2)^2$ for $r \equiv |\mathbf{r}| \leqslant 1$ and zero otherwise. The weights w_i are calculated using a lognormal Chabrier (2001) model for the IMF and a constant SFH. The parameter h is the kernel size, set to $N^{-1/5}$, where N is the number of training points, following "Scott's rule" (for one-dimensional data, as we are primarily interested in the one-dimensional distribution $p(M_{K_s}|J - K_s)$; Scott 1992), and λ_i is a local bandwidth factor, calculated as

$$\lambda_i = \left(\frac{\hat{p}(\mathbf{x}_i)}{s}\right)^{\alpha}, \tag{5}$$

where $\hat{p}(\mathbf{x})$ is an estimate of the density distribution, s is the (straight) geometric mean of the density over $\mathbf{x}_i$: $\log s = \sum_i \log \hat{p}(\mathbf{x}_i)/N$, and $\alpha = 0.5$. We iterate three times to calculate the weights λ_i, starting from uniform λ_i.

The resulting CMD is shown in the top panels of Figure 2 for four values of the overall metallicity Z. The CMD in this figure has been normalized independently for each color to produce the conditional probability distribution function (PDF); this approach demonstrates the dependence of the RC absolute magnitude on color at a given metallicity. The lines show the peak and half-maxima as a function of color. In these diagrams, the interval between the dashed lines where the absolute-magnitude PDF is extremely sharply peaked corresponds quite well to the color interval for which, at that given metallicity, He-burning stars are old enough (roughly >1.5 Gyr) to be in a compact, "classical" RC; this feature naturally results from all these He-burning stars having developed a degenerate core of similar mass earlier in their evolution as RGB stars. To the blue of this interval, the mean magnitude abruptly falls by ≈0.4 mag, and becomes far from constant at even bluer colors; this is essentially the behavior expected from secondary red-clump stars, which have ignited He in non-degenerate conditions (Girardi 1999). The magnitude distribution at even bluer colors, and at colors redder than the reddest dashed line, becomes significantly more extended and featureless; those intervals no longer reflect the behavior of He-burning stars, but rather those of main-sequence, RGB, and asymptotic giant-branch (AGB) stars.

We calculate the theoretical CMD in this manner for metallicities on a grid with spacing $\Delta Z = 0.0005$ and determine the peak M_{K_s} and FWHM as a function of color. The result is presented in Figure 3, where the FWHM has been converted into the equivalent Gaussian standard deviation σ. This figure clearly shows the region in the $(J - K_s)_0$ and Z plane where the magnitude PDF has $\sigma \lesssim 0.1$ mag, i.e., where distances precise to 5% can be determined spectro-photometrically. However, it is clear that this locus is strongly dependent on metallicity. The dashed lines approximately bound the low-σ locus; they are given by

$$Z > 1.21\,[(J - K_s)_0 - 0.05]^9 + 0.0011 \tag{6}$$

$$Z < 2.58\,[(J - K_s)_0 - 0.40]^3 + 0.0034, \tag{7}$$

with additional bounds of

$$Z \leqslant 0.06, \quad (J - K_s)_0 \geqslant 0.5. \tag{8}$$

The width of the magnitude distribution near the edges of this region increases to 0.2 mag, which still yields 10% precision in the derived distances. As discussed in Section 2.1, the contribution to the distance uncertainty from errors in the extinction correction is typically 0.05 mag, smaller than the intrinsic spread in the RC luminosity. Equations (6)–(8) are highly effective at eliminating secondary red-clump, RGB, and AGB stars from the sample.

Figure 3 also demonstrates that the peak magnitude of the PDF does not depend strongly on either color or metallicity, with a minimum-to-maximum variation of about 0.2 mag. We have also computed the surface in Figure 3 assuming an exponentially declining star-formation rate or a Kroupa (2003) IMF. The difference with respect to our fiducial assumptions is presented in Figure 4. This figure shows that there are only minor differences within the region of our color and metallicity cuts, especially for the peak of the magnitude PDF. Assumptions about the SFH or IMF therefore do not introduce appreciable systematics, with offsets typically less than 1% in distance.

We have also computed the density near the RC using the Padova (Girardi et al. 2000; Bonatto et al. 2004) and BaSTI (Pietrinferni et al. 2004) isochrone libraries using the same IMF and SFH assumptions. For the latter, we combine the transformations of Carpenter (2001) and Bessell & Brett (1988) to transform the BaSTI K magnitudes to 2MASS K_s magnitudes. The conditional density $p(M_{K_s}|[J - K_s]_0)$ for four different

[40] In the discussion of the KDE modeling of the CMD we always assume that $J - K_s$ is dereddened, but we do not add the superscript "0" to avoid notational clutter.

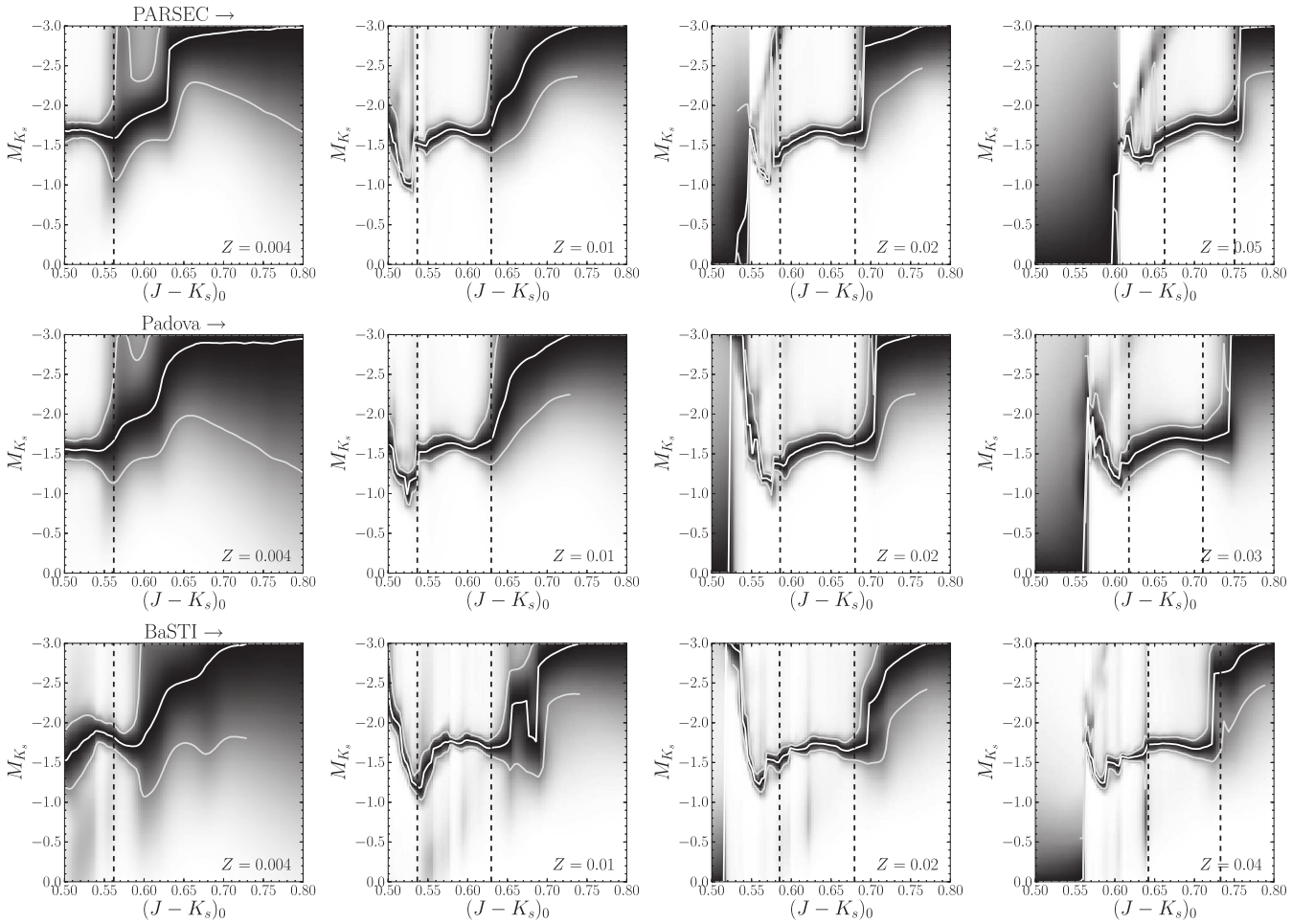

Figure 2. Conditional PDF $p(M_{K_s}|[J-K_s]_0)$ for stars satisfying the cuts in Equations (2) and (3). This PDF is computed using the KDE method and SFH and IMF assumptions described in the text, for different metallicities (horizontally; the last column shows the highest metallicity Padova and BaSTI models and a high-metallicity PARSEC model) and different stellar evolution codes (PARSEC, upper panels; Padova, middle panels; BaSTI, bottom panels). The middle white line marks the peak of the PDF and the outer white lines indicate where the PDF reaches half of its maximum. At each metallicity there is a color range where the PDF is extremely narrow. The vertical dashed lines in each panel show the color cuts of Equations (6) and (7) that isolate the range over which the magnitude distribution is narrow. The color range and morphology of this locus is similar for the different stellar evolution codes and the dashed lines bound the locus with a narrow magnitude range for the three different codes.

metallicities for these alternative isochrone models is also shown in Figure 2. It is clear that the Padova densities are similar to those obtained from the PARSEC isochrones, especially in the region where the color–magnitude locus is narrow. A detailed comparison between the peak and FWHM of the magnitude PDF shows that the Padova and PARSEC isochrones give the same color–metallicity region over which the RC is narrow; the color-dependence of the peak magnitude is the same for the two models (the Padova isochrones' maximum metallicity is $Z = 0.03$).

For the BaSTI isochrones we only use the values $Z = [0.004, 0.008, 0.01, 0.0198, 0.03, 0.04]$ provided by BaSTI and do not use adjacent metallicity bins to increase the model sampling, as we do for Padova and PARSEC models (the BaSTI models are sampled for a much larger number of initial masses). Figure 2 shows that the RC locus at high metallicity is similar to that obtained from Padova and PARSEC models.

Giants on the RGB are affected by mass loss, the details of which are not completely understood. Mass loss is a few times $0.01\,M_\odot$ for giants with ages $\lesssim 5$ Gyr and so is largely negligible, but older giants can loose a few times $0.1\,M_\odot$ (e.g., Reimers 1975; Schröder & Cuntz 2005). However, mass loss essentially only affects the mass in the stellar envelope and the core mass that ignites He is unaffected, such that the effect on the RC luminosity is small. The PARSEC models use the Reimers law for mass loss with an efficiency parameter of $\eta = 0.2$ (e.g., Miglio et al. 2012), while the Padova and BaSTI models use $\eta = 0.4$. The good agreement among the different stellar isochrones in the RC region therefore explicitly demonstrates that the details of mass-loss prescriptions are unimportant. Additionally, we have computed the peak magnitude of the RC for $\eta = 0.1$ and $\eta = 0.3$ (roughly the range allowed by Miglio et al. 2012) and find that the magnitude solely changes at the red end of the RC and only by <0.02 mag. The effect on the RC distances is therefore negligible.

The models that we used in this section to characterize the RC locus are all solar-scaled models. One of the main motivations of APOGEE is to explore elemental abundance ratios beyond the overall metallicity and therefore we need to understand how the RC locus changes when abundances are not solar scaled. In Figure 5, we present the conditional PDF $p(M_{K_s}|[J-K_s]_0)$ for stars satisfying the cuts in Equations (2) and (3) for two models that are enhanced in α elements with respect to the solar ratios. We employ BaSTI models with $[\alpha/\mathrm{Fe}] = 0.4$ (Pietrinferni et al.

2006) with an overall metallicity of $Z = 0.01$ and $Z = 0.02$; [Fe/H] for these models is about 0.35 dex lower than for the equivalent solar-scaled models. These α-enhanced models are moved blueward because of the decreasing Fe opacity for α-enhanced models at fixed overall metallicity. In the relevant metallicity range for α-enhanced stars ($-1 \lesssim$ [Fe/H] $\lesssim 0$), the blueward shift is $\approx$0.025 mag.

The metallicity presented in the APOGEE catalog that we use for the basis of the RC selection is calibrated to [Fe/H] rather than the overall metallicity. Therefore, when we calculate Z([Fe/H]) below for applying the cuts in Equations (6) and (7), we are underestimating the overall metallicity for α-enhanced stars. The bias in $\log Z$ is approximately 0.35 dex ([α/Fe]/0.4 dex). Therefore, the (color,metallicity) cut for a true RC stars at a given ($[J - K_s]_0$, $\log Z$) will be evaluated at the wrong ($[J - K_s]_0$, $\log Z - 0.35$ dex) and we might spuriously remove some of the reddest RC stars because the RC cuts shift blueward for lower metallicity stars. This is problematic as the red part of the RC is where the oldest stars (ages $\gtrsim$5 Gyr) are located and these old stars are the ones that could be α-enhanced. However, the blueward shift of the true RC locus with [α/Fe] means that we do not loose many stars. The red cut in Equation (6) has a slope in ($[J - K_s]_0$, $\log Z$) of $\approx$6 dex mag^{-1}. From inspecting the isochrone models for old stars, we find that our cuts at low Z are such that old stars are typically selected $\approx$0.02 mag bluer than the red cut of Equation (6). Therefore we do not remove true RC stars with [α/Fe] $\lesssim$ 0.25 dex. Only 8% of stars with [Fe/H] > -1, $T_{\rm eff} > 4200$ K and [α/Fe] > 0.05 have [α/Fe] > 0.25 in the first two years of APOGEE data. Therefore, [α/Fe]-bias in the RC selection at high [α/Fe] is small.

The different isochrone models do not entirely agree on the absolute magnitude of the RC, with PARSEC isochrones having a near-uniform offset of $\sim$0.1 mag and $\sim$0.05 mag with respect to the Padova and BaSTI models, respectively. This result shows the need to externally calibrate the brightness of the RC. However, the offset is small and would only lead to systematics of order 5% or less in distance.

2.3. Contamination by RGB Stars

The RC selection technique presented in this section requires highly accurate and precise measurements of $\log g$. Using the APOKASC data, we can evaluate how well the selection technique works for various precisions in $\log g$. We can estimate the contamination by applying the selection to those stars in the APOKASC catalog for which the evolutionary state was obtained by Stello et al. (2013; which therefore provides the ground truth of whether a star is in the RC or not). Using the $\log g_{\rm seismo}$ measurements from asteroseismology, the contamination of non-RC stars is 4 ± 2%. This is therefore the best that the presented technique can do. Using more realistic errors of 0.1 dex and 0.2 dex in $\log g_{\rm spec}$ from the analysis of high-resolution spectra, the contamination rises to 9 ± 2% and 14 ± 3%, respectively. This contamination can be compared, for example, to the selection technique used by Williams et al. (2013), which consists of the simpler cuts $0.55 \leqslant (J - K)_0 \leqslant 0.8$ and $1.8 \leqslant \log g \leqslant 3.0$. Applying these cuts to $\log g_{\rm seismo}$ yields a contamination of 33 ± 3%, eight times larger than the contamination for the new technique presented here. Using RAVE (Steinmetz et al. 2006) data with spectroscopic $\log g$, Williams et al. (2013) estimate their contamination to be $\approx$60%.

For the current spectroscopic pipeline for APOGEE, the errors in $\log g$ are approximately 0.2 dex, but there are systematic offsets in the measured $\log g_{\rm spec}$ for RC and RGB stars that are such that the RC and RGB are closer together by $\approx$0.2 dex, making it more difficult to separate them. From the Stello et al. (2013) sample, the contamination by RGB stars using the current APOGEE $\log g_{\rm spec}$ is 23 ± 3%. Improved analysis of the APOGEE spectra should in the future remove the relative bias in $\log g$ for RC and RGB stars.

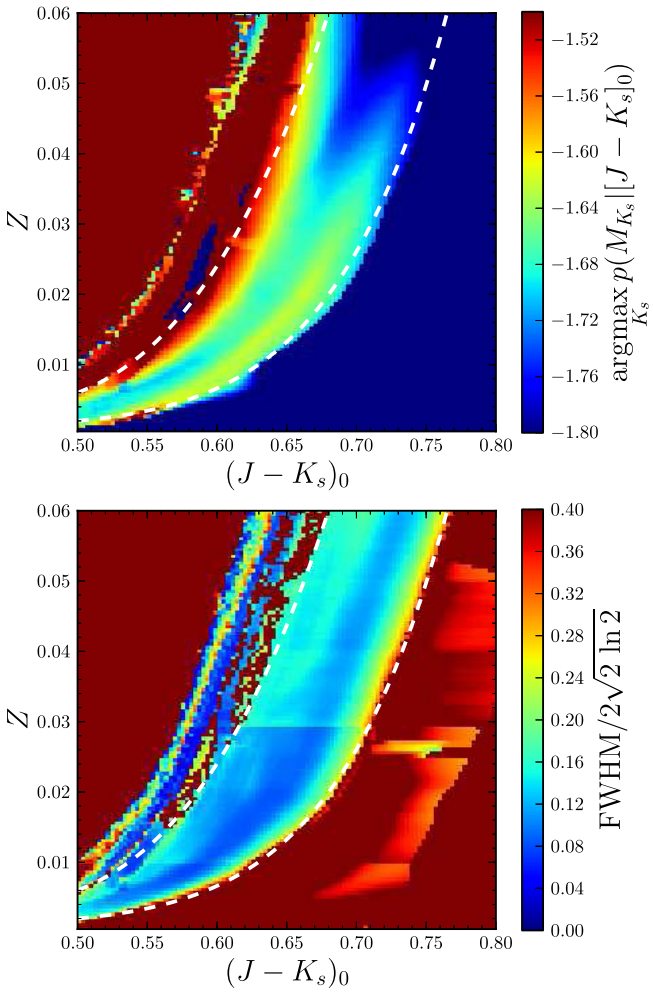

Figure 3. Peak of the magnitude PDF $p(M_{K_s}|[J - K_s]_0)$ as a function of color and metallicity Z for PARSEC isochrones (top panel). The bottom panel shows the FWHM$/2\sqrt{2\log 2}$ ($\approx\sigma$) of the PDF. The white dashed lines represent the region specified by the cuts in Equations (6) and (7) over which the distribution of absolute magnitudes is narrow. The peak of the magnitude PDF does not strongly depend on color or metallicity over the region where the PDF is narrow.
(A color version of this figure is available in the online journal.)

The current bias in the relative $\log g$ measurements of RC and RGB stars is such that $\log g$ starts to be underestimated for RGB stars below around $T_{\rm eff} = 4900$ K (see M. Pinnsoneault et al., in preparation). Practically, this means that we must change the upper $\log g$ limit used to define the RC sample to take into account the biased $\log g$ measurements for the RGB stars. This can be done by specifying the following additional cut that follows the $\log g$ bias as a function of $T_{\rm eff}$

$$\log g < 0.001 \text{ dex K}^{-1} (T_{\rm eff} - 4800\,\text{K}) + 2.75. \quad (9)$$

In the current SDSS-III's Data Release 11 (DR11; years one and two) sample (see below), this cut removes 2,261 out of 12,613 catalog objects, or about 18% of the sample. Using the APOKASC sample we find that this additional

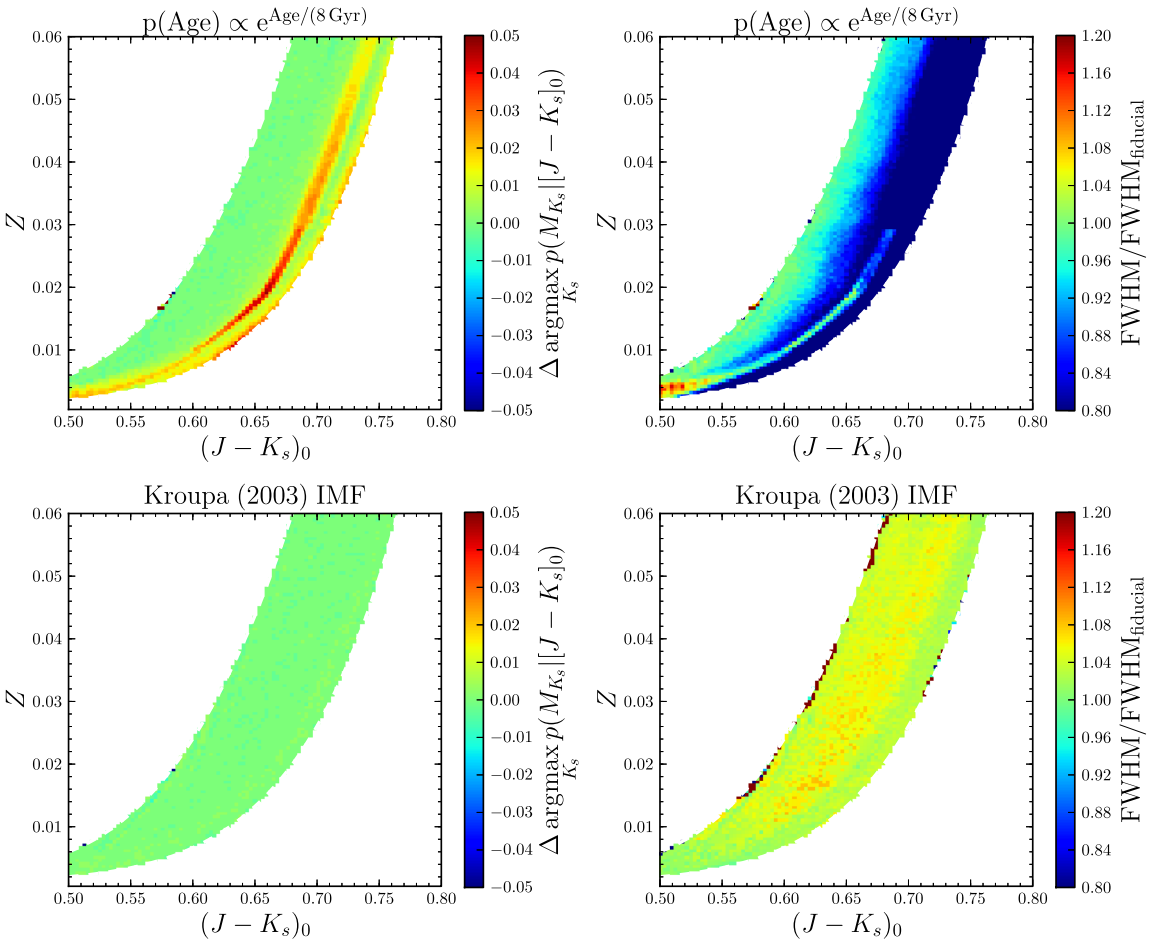

Figure 4. Variation of the peak and width of the magnitude PDF $p(M_{K_s}|[J-K_s]_0)$ for an exponentially declining star-formation rate or a Kroupa (2003) IMF. This figure shows the difference (absolute for the peak magnitude, relative for the width) between the results obtained using these alternative assumptions and our fiducial model (lognormal Chabrier 2001 IMF and constant SFH). We only display the comparison in the RC region defined by the cuts in Equations (6) and (7). The deviations in the mean magnitude are typically $\lesssim$0.02 mag or $\lesssim$1% in distance. The distribution of absolute magnitudes has the same small width to within $\approx$10% regardless of the IMF or SFH chosen.

(A color version of this figure is available in the online journal.)

constraint reduces the contamination to 10% ± 3% compared to 23% contamination without this extra cut. We stress that this additional cut is a temporary solution to the ASPCAP problems with the relative $\log g$ of RC and RGB stars. Once this bias is removed by pipeline improvements, the additional $\log g$–$T_{\rm eff}$ constraint will no longer be necessary. However, it can still be applied to obtain a sample of RC stars with extremely high purity: Using the APOKASC sample with evolutionary state measurements, we estimate that applying the cut in Equation (9) reduces the contamination from 14% to less than 5% and 10% for $\log g$ uncertainties of 0.1 dex and 0.2 dex, respectively.

We stress that the contamination fractions discussed in the previous paragraphs are estimates; the true contamination could be different if the sample of APOKASC stars with evolutionary-state measurements does not accurately represent the parent APOKASC sample, or if the APOKASC sample does not reflect the RC and RGB populations in the *Kepler* field (Koch et al. 2010) or in other parts of the Galaxy.[41] By comparing the Stello et al. (2013) sample to the parent APOKASC sample we find that we are likely slightly overestimating the contamination from RGB stars, as RGB stars near the RC locus are disproportionally represented in the sample for which the evolutionary state has been measured: 23% of the stars between the dashed lines in Figure 1 versus 33% of the stars below the high-$\log g$ line have measurements of their evolutionary state, which implies that the contamination fraction in the full APOKASC sample is likely $\approx$40% smaller at 7% ± 2% rather than 10%. However, the APOKASC sample itself was constructed using a complicated combination of cuts by *Kepler* to create the asteroseismic sample of giants and by the APOKASC collaboration to provide spectroscopic follow-up for a subset of these (see M. Pinnsoneault et al., in preparation). Therefore, the relation between the APOKASC catalog and the underlying Galactic populations is hard to quantify. APOKASC preferentially selected first-ascent red giants for spectroscopic follow-up, such that RGB stars are overrepresented compared to RC stars in the asteroseismic sample and the 7% contamination fraction is probably still an overestimate.

To summarize our RC selection and characterization technique: We select RC stars using the cuts in Equations (2), (3), (6), (7), and (8). Because of the current ASPCAP bias in the relative $\log g$ measurements of RC and RGB stars, we also apply the cut in Equation (9), although this additional cut

[41] Additionally, the Stello et al. (2013) sample contains only a few stars with enhanced [α/Fe] with respect to the solar value. Therefore, we cannot currently test the RC selection for α-enhanced stars. We will describe the outcome of tests with such stars in updates of the RC catalog, when seismological classifications become available for such stars.

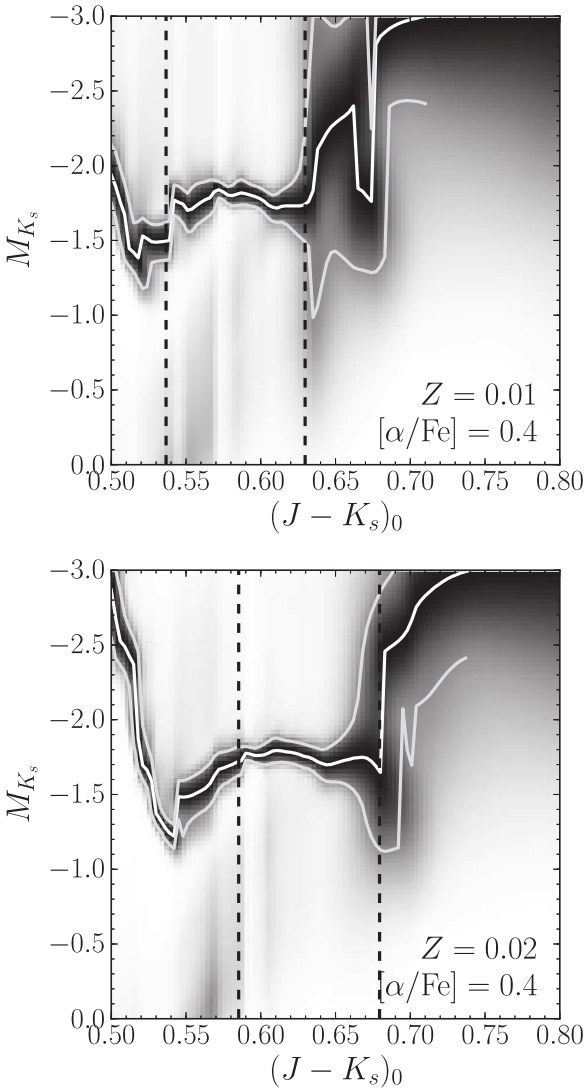

Figure 5. Effect of α-enhancement on the RC locus. This figure shows the same conditional PDF $p(M_{K_s}|[J-K_s]_0)$ for stars satisfying the cuts in Equations (2) and (3) for BaSTI models as in Figure 2, except that the models have $[\alpha/\mathrm{Fe}] = 0.4$. The iron abundance [Fe/H] in these models is ≈0.35 dex lower than for the equivalent non-α-enhanced models. The dashed lines are the cuts in Equations (6) and (7) calculated based on the total metallicity Z. The RC locus is shifted approximately 0.025 mag blueward for α-enhanced models compared to solar-scaled models with the same overall metallicity.

will no longer be necessary once the ASPCAP bias in $\log g$ is removed by improved modeling of the APOGEE spectra. For stars satisfying these constraints, we calculate the absolute K_s magnitude from the dereddened color $(J-K_s)_0$ and the metallicity Z using the two-dimensional surface in the top panel of Figure 3. In Section 3, we discuss the uniform calibration offset that is applied to these individual absolute magnitudes to place the distances on the *Hipparcos* scale.

3. DISTANCE CALIBRATION

We calibrate the absolute magnitude of the PARSEC stellar-isochrone models for the RC discussed in the previous section by using them to calculate the average absolute magnitude for a RC sample of stars that mimics that found close to the Sun. The average absolute K_s magnitude of nearby RC stars is well-calibrated using *Hipparcos* parallaxes (e.g., Alves 2000; Groenewegen 2008; Laney et al. 2012). Our standard model for a sample of stars that resembles local stars is a population that has a distribution of metallicities similar to that found by Casagrande et al. (2011) (with their $p([\mathrm{Fe/H}])$ approximated here as a mixture of two Gaussians with relative weights 0.8 and 0.2, means of 0.016 dex and −0.15 dex, and dispersions of 0.15 dex and 0.22 dex, respectively) and a constant star-formation history with a lognormal Chabrier (2001) IMF. The average K_s absolute magnitude of such a population as predicted by PARSEC is −1.65.

We choose the recent Laney et al. (2012) calibration of $M_{K_s} = -1.61$ of local RC stars, which is in very good agreement with the results of Alves (2000), but is 0.07 mag brighter than the calibration of Groenewegen (2008). Therefore, there is a 3.5% systematic distance offset between distances derived from these two calibrations. The calibration of Laney et al. (2012) is more accurate than that of Groenewegen (2008) because they re-measure the magnitudes of bright RC stars that are saturated in 2MASS ($K \lesssim 5$); their calibration is accurate to 2%.

Because the PARSEC models predict an average K_s absolute magnitude that is 0.04 mag brighter than that found from local observations, we apply a uniform 0.04 mag correction to the individual K_s magnitudes determined using the PARSEC models based on a star's ($[J-K_s]_0$, Z) in Figure 3 when calculating distances for the sample of RC stars in APOGEE. This correction does not strongly depend on the assumptions made about the age and metallicity composition of a local population of stars. Figure 6 shows the correction for different assumptions about the age and metallicity distribution. For a reasonable metallicity distribution, the systematic differences are below 0.01 mag, or less than 0.5% in distance.

We can further test the distance calibration using the APOKASC sample by calculating "direct seismic" distances using spectroscopic $T_{\rm eff}$, stellar radii determined using asteroseismic scaling relations, and bolometric corrections (e.g., Marigo et al. 2008) (see T. Rodrigues et al., in preparation, for full details); these distances have random and systematic uncertainties of 5% each (Miglio et al. 2013). Using $\log g_{\rm seismo}$ and the procedure described in Section 2 to select RC stars, we compare the seismic with the RC distances (including the *Hipparcos* calibration) for 593 stars and find that the seismic and RC distances agree to within better than 1% using the median difference, with a scatter of ≈7%. For the subset of APOKASC stars with evolutionary state measurements (see section 2.3), the scatter is only 5%. Similarly, we compare the RC distances with the seismic distances from the SAGA catalog (Casagrande et al. 2014). For the 42 stars in common between the sample of 593 APOKASC RC stars and the SAGA sample, the seismic distances agree with the RC distances to within $3\% \pm 1\%$, with a scatter of 6%.[42] These values are consistent with each method's random and systematic uncertainties and show that our distance calibration is sound.

We therefore conclude that the distances that we assign to RC stars are unbiased to within ≈2% and have random uncertainties of ≈5%. The distance distribution of the 10,341 RC stars selected using the method described in Section 2 from DR11 of APOGEE is presented in Figure 7 (see Section 6 for full details on this sample). Many of the RC stars in the sample are only a few kiloparsecs from the Sun, with a median distance of 2.75 kpc and a 95% interval of 0.8 kpc and 6 kpc. The distribution of this sample in Galactocentric coordinates is shown in Figure 8. This

[42] T. Rodrigues et al., in preparation, also show that their seismic distances agree to better than 1% with the seismic distances in the SAGA catalog by considering all giants in common between the two samples.

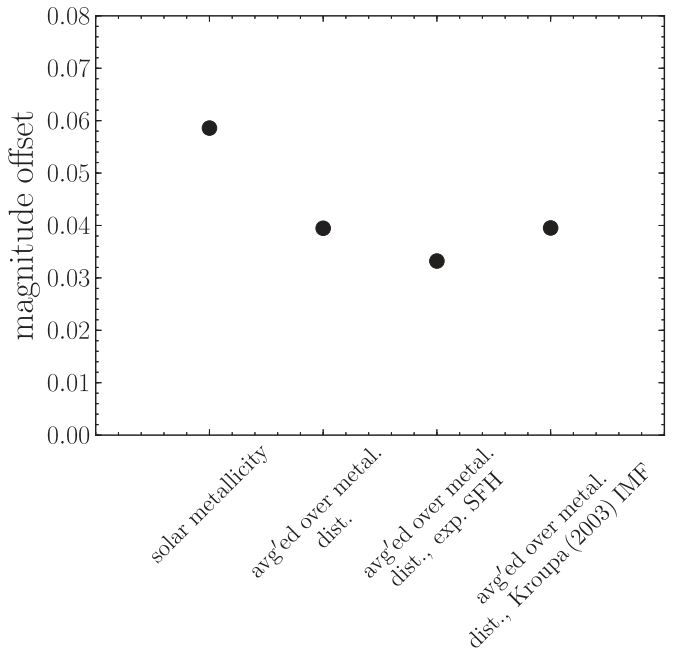

Figure 6. External calibration of the absolute magnitude scale of the RC: This figure shows the difference between the average RC magnitude derived from *Hipparcos* data (Laney et al. 2012) and the mean RC magnitude calculated by averaging the peak magnitudes of the PARSEC RC over color and metallicity. The first point is the difference when using only the solar metallicity isochrones, while the other points are averaged over the metallicity distribution of local stars (Casagrande et al. 2011). The second point assumes a constant star-formation rate and a lognormal Chabrier (2001) IMF, while the third and fourth points assume an exponentially declining star-formation rate and a Kroupa (2003) IMF, respectively. The assumptions about the star-formation history and IMF affect the magnitude calibration at a level that is below a percent.

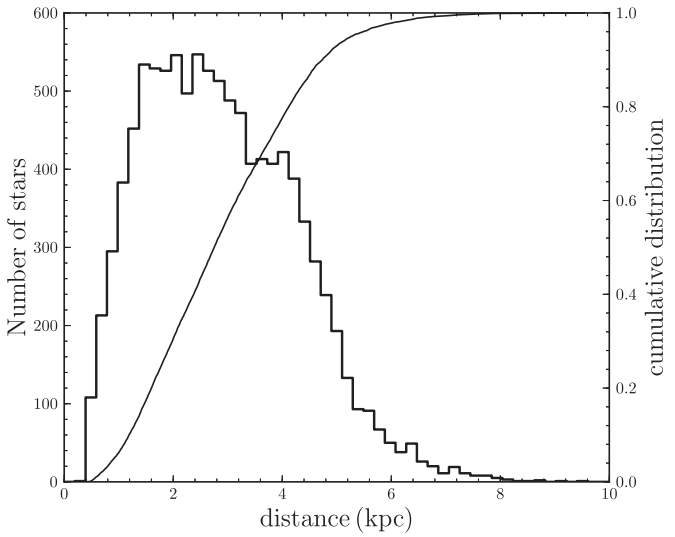

Figure 7. Distance distribution of the 10,341 stars in the DR11 APOGEE-RC sample (histogram). The solid line shows the cumulative histogram. The median distance is ≈2.75 kpc and 90% of the stars lie between 1 and 6 kpc.

shows that the sample spans a large area of the Galactic disk near the midplane.

4. SAMPLE SELECTION FUNCTION

As a spectroscopic survey observing a relatively small number of objects in the photometric 2MASS catalog, APOGEE requires decisions as to what lines of sight to observe, what types of stars to target in the chosen directions, and how to sample these stars as a function of their photometric properties. These decisions affect how the underlying photometric sample is reflected in the spectroscopic data. To connect the high-dimensional distribution (or moments thereof) of positions, velocities, and elemental abundances found in the spectroscopic sample to the distribution of all stars it is necessary to correct for the effects of the selection (often referred to as selection biases), beyond the obvious angular selection function encased in the APOGEE pointings (e.g., Figure 9). Generally, the relation between the spectroscopic sampling on the underlying Galactic population can be divided into three parts (see Section 4 of Rix & Bovy 2013): (1) the procedure by which the survey selects stars from all potential targets, (2) the relation between the kinds of stars observed and the full underlying stellar population, and (3) the relation of the observed spatial volume (typically a small number of lines of sight) to the global volume. The last point requires one to extrapolate the observed stellar distribution in the observed lines of sight to the large volume between lines of sight; one must assume that spatial gradients in the underlying distribution are well sampled by the observed lines of sight, and one needs to estimate these gradients, which can be done by modeling the spatial dependence of the stellar distribution within the observed field pointings. However, as this last step requires extensive modeling of the observed distributions, we do not discuss it here further (see Bovy et al. 2012b, 2012d for an example of this procedure).

We discuss the selection effects of (1) and (2) in this section and the next, respectively. The overall APOGEE sample contains dozens of sub-samples selected for a variety of reasons (e.g., observations of members of stellar clusters or the Sgr dwarf galaxy, observations of stars in the *Kepler* field for which asteroseismology data exist, etc.), most of which do not provide a fair sample in any sense of the large-scale Galactic distribution of stars. However, most APOGEE targets are selected using a simple color cut, $(J - K_s)_0 \geqslant 0.5$, typically in three separate H-band magnitude ranges (Zasowski et al. 2013), and this simple selection allows the fraction of spectroscopically-observed objects to be determined as a function of color $(J - K_s)_0$ and magnitude H. We will refer to this sample as APOGEE's main sample, reserving the name statistical sample for the part of the main sample for which observations are complete (defined as the observations having a signal-to-noise ratio of 100 per half-resolution element).

For the purposes of describing the details of the APOGEE target selection, it is necessary to give a brief description of the basic data-collecting process (see also the Glossary in Appendix A of Zasowski et al. 2013). APOGEE observes stars in a set of *fields*, which are circular locations on the sky with a radius of 1.°49; see Figure 9 for the location of all of these fields. Fields are observed in one "visit" sessions for up to 24 visit; each visit consists of a ≈64 mins observation. The vast majority of fields are observed for three visits only, some fields are observed for only one visit (most fields in the *Kepler* field, most fields in the Galactic bulge, and fields targeting the core of the Sgr dwarf galaxy), and others are observed for 6, 12, or 24 visits. The main sample for fields observed for three visits or less consists of a single magnitude cohort. Other fields have either two or three magnitude cohorts, corresponding to two or three magnitude ranges. Typically, the brightest cohort, known as the short cohort, has $7.0 \leqslant H \leqslant 12.2$, the intermediate medium cohort has $12.2 < H \leqslant 12.8$, and the long cohort has

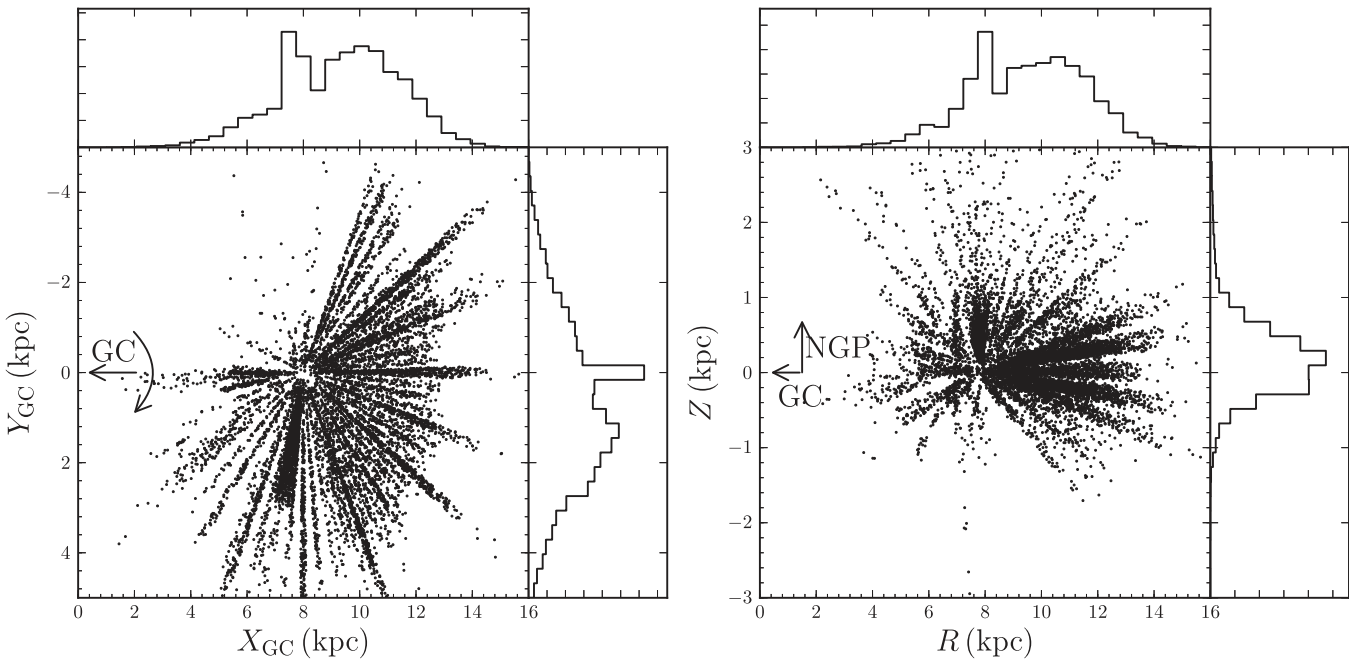

Figure 8. Distribution of the 10,341 stars in the DR11 APOGEE-RC sample in Galactocentric coordinates: distribution in the plane (left panel) and in Galactocentric radius and distance from the plane (right panel). The Sun is located at $(X_{GC}, Y_{GC}, Z) = (8, 0, 0.025)$ kpc. The overdensity of stars near $X_{GC} = 8$ kpc and $R = 8$ kpc is due to a large concentration of APOGEE targets in the *Kepler* field.

$12.8 < H \leqslant 13.3$ or 13.8, depending on whether the field is observed for 12 or 24 visits; we refer to this cohort distribution as the standard cohort distribution. The main exceptions to this rule are fields with a single one-visit cohort, for which the short cohort has $7.0 \leqslant H \leqslant 11$; some of the bulge fields with a single-visit cohort have a medium cohort that has $11.0 < H \leqslant 12.2$. To a good approximation, we can assume that within each cohort's magnitude range, the color and magnitude are sampled uniformly from the underlying population.[43] For the purpose of the discussion, we will assume the standard cohort distribution.

In fields observed for six visits or more, there are multiple three visit short cohorts (one for every three visits), and for fields observed for 12 visits or more there are multiple medium cohorts (one for every six visits); there is only ever a single long cohort per field. A design consists of a three-visit set of targets: this contains a short cohort with a unique set of targets, a medium cohort with targets shared among two designs, and a long cohort with targets shared among all designs for a given field (see Figure 1 in Zasowski et al. 2013 for a visual representation of different designs for a given field). A three visit field has a single design; a six visit field has two designs, with a different short cohort on each design and a shared medium cohort; and a 12 or 24 visit field has four or eight designs, with four or eight unique short cohorts, two or four medium cohorts, and a single long cohort. Each design is implemented as a set of spectroscopic plates, which corresponds to a physical plug-plate loaded onto the telescope. A design may be used on a single plate or on multiple plates. Plates are observed in one-visit increments. For the purpose of determining the selection function, we only consider plates for which all planned observations were complete by the deadline for DR11 (2013 August 1). Figure 9 shows the fraction of completed plates for short, medium, and long cohorts out of all planned plates as part of APOGEE's three-year run. Near the disk, observations have high completeness, except for the region $30^\circ \lesssim l \lesssim 100^\circ$.

Using the mapping between plates, designs, and cohorts, we can determine for which fields and cohorts all of the observations for a set of stars are complete. As an example, for a 12 visit field, we can determine which of its four different short-cohort sets of targets have been observed to completion, the same for its two different medium-cohorts sets of targets, and for its single long cohort. For the purpose of building a statistical sample, we then ignore all spectroscopic targets for which observations have not reached the full exposure time (such stars are present in the APOGEE data products). For each combination of a field and a cohort's magnitude range APOGEE provides a random sampling of the underlying photometric sample. The selection function for a field and magnitude-range combination is therefore simply given by the number of stars in the statistical sample in this field and magnitude range, divided by the number of stars in the photometric sample in the same field and magnitude range. For example,

$$\text{selection fraction (field X, } 7.0 \leqslant H \leqslant 12.2) = \frac{\text{No. of stars in stat. sample in field X, with } 7.0 \leqslant H \leqslant 12.2}{\text{No. of stars in phot. sample in field X, with } 7.0 \leqslant H \leqslant 12.2} \quad (10)$$

and similarly for the medium and long magnitude ranges for each field. Thus, for each field the selection function is piecewise constant with jumps at the magnitude limits of the (up to three) cohorts of each field.

To determine whether the piecewise-constant model for the selection function is a good approximation, we compare the magnitude distribution of stars in the statistical spectroscopic

[43] In detail, the sampling is random in three bins, each containing 1/3 of the stars, in the short cohort; in the medium and long cohorts each N-th star is observed, with N chosen such as to provide the desired total number of targets in each cohort. While these schemes are not entirely random, the large number of stars combined with the 2MASS magnitude errors and some stars not being observed because of practical observational reasons serve to make this sampling nearly indistinguishable from a random sampling (see Figure 10).

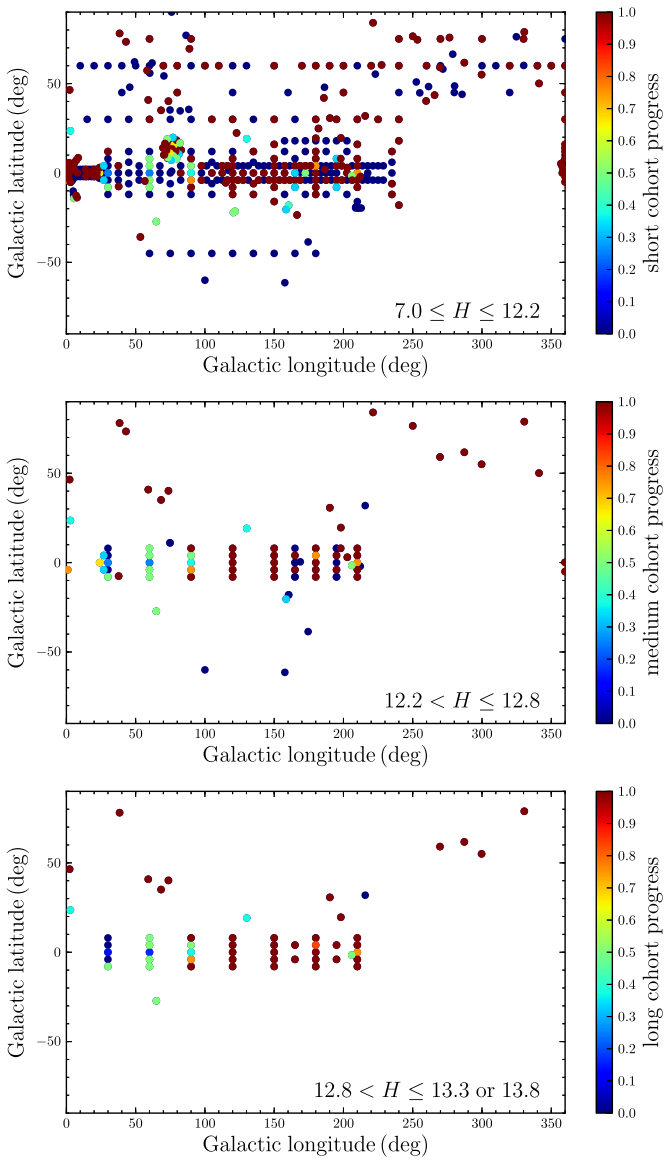

Figure 9. APOGEE's target completeness in different fields after the first two years. The different panels show the fractional completeness for different fields on the sky for "short" cohorts (top panel), "medium" cohorts (middle panel), and "long" cohorts (bottom panel); see text for the meaning of the different cohorts. Overall, short cohorts are 50% complete, medium cohorts 66%, and long cohorts 78%. The *H*-band limits do not apply to all fields; some fields have a short cohort with $7.0 \leqslant H \leqslant 11.0$ and some of those have a medium cohort with $11.0 \leqslant H \leqslant 12.2$ (this applies in particular to most bulge plates around $l = 0°$ and all *Kepler* fields around $(l, b) = (75°, 15°)$).

(A color version of this figure is available in the online journal.)

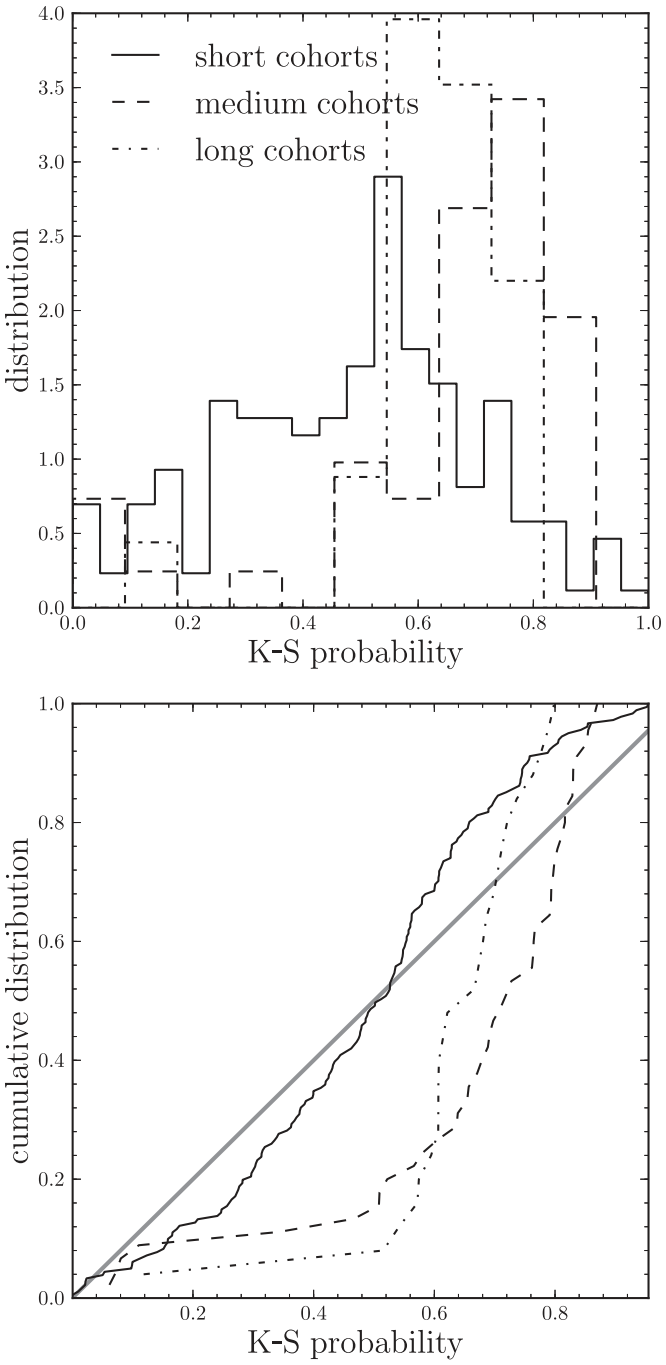

Figure 10. Distribution of the K-S probability that a field/cohort combination's statistical spectroscopic sample was drawn from the underlying photometric sample combined with the model selection function. This calculation is shown separately for short, medium, and long cohorts. The bottom panel shows the cumulative distribution. All field/cohort combinations have a large probability that their statistical spectroscopic sample was drawn from the underlying photometric sample, with the few field/cohort combinations with low probability consistent with statistical fluctuations (i.e., close to the one-to-one line in the cumulative distribution panel, shown in gray).

sample to that of stars in the photometric sample within the same field and magnitude range. This comparison is done for the up to three different cohort-magnitude-ranges of each field separately. In each field and magnitude-range combination, the selection function model is that the statistical sample is a fair sampling of the underlying photometric distribution of targets, and this model is tested by computing the Kolmogorov–Smirnov (K-S) probability that the statistical sample distribution of *H*-band magnitudes is the same as that of the photometric sample.

A histogram of these probabilities is shown in Figure 10. The vast majority of K-S probabilities of the short cohorts are large, such that the hypothesis that the statistical sample was drawn from the photometric sample cannot be rejected; the few fields whose short cohort has a small K-S probability are consistent with random noise (out of 102 short cohorts, one expects ≈5 to have a K-S probability <0.05 and we find 4). The medium and long cohorts also mostly have large K-S probabilities, with the 1 out of 41 medium cohorts and 0 out of 25 long cohorts with $P_{\text{K-S}} < 0.1$, consistent with

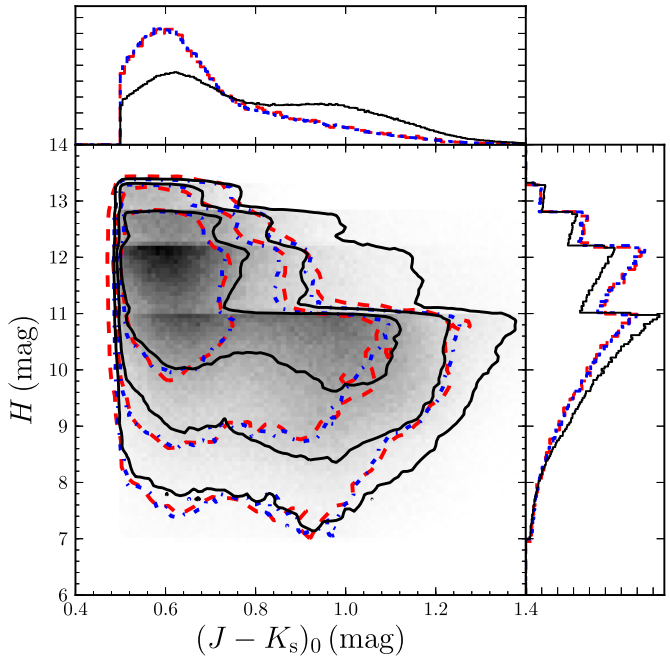

Figure 11. Color–magnitude sampling of the statistical sample. The linear grayscale and the black lines show the density of potential targets in fields and cohorts contained in the statistical sample. The red dashed lines represent the distribution of stars in the statistical spectroscopic sample and the blue dash-dotted lines display the distribution of potential targets re-weighted by the selection function (see Equation (10) and related discussion). The contours contain 68%, 95%, and 99% of the distribution. The re-weighting of the photometric sample using the selection function perfectly reproduces the color–magnitude sampling provided by the statistical spectroscopic sample.

(A color version of this figure is available in the online journal.)

random statistical fluctuations. We therefore conclude that the piecewise-linear model of Equation (10) is a good model for the selection function. We do caution that the K-S probabilities of medium and long cohorts are somewhat too consistent with the underlying distribution, which likely results from the non-random "N"th-star sampling used (see footnote 41) for these cohorts. However, due to photometric magnitude errors, the spectroscopic sampling is still an effectively random sampling of the intrinsic magnitude distribution (i.e., that which one would observe without errors).

The distributions in color $(J-K_s)_0$ and magnitude H of the photometric sample in fields and magnitude ranges contained in the statistical sample are shown as the density grayscale and black contours and histograms in Figure 11. This distribution clearly shows the influence of the cohort magnitude limits at $H = 11$, 12.2, 12.8, and 13.3 (there are currently no completed 24 visit fields that would reach $H = 13.8$). The fiber allocation to different cohorts is such that stars in the fainter magnitude bins are over-represented with respect to the brightest bin, such that the magnitude distribution as well as the color distribution of the statistical sample (shown as red dashed contours and histograms) is weighted to fainter magnitudes and bluer colors. The latter happens because, even though the color sampling is random over the same color range for all magnitude ranges, the intrinsic correlation between color and magnitude in the photometric sample leads to an apparent bias in the color distribution of the spectroscopic sample. Using the model for the selection function described above, we can re-weight stars in the photometric sample such that they trace the sampling of the spectroscopic sample, and this distribution is shown as blue dash-dotted contours and histograms. It is clear that correcting for the selection function leads to perfect agreement between the re-weighted photometric sample and the statistical spectroscopic sample.

The selection function is a function of location on the sky (field location, or equivalently, Galactic longitude and latitude) and H-band magnitude. To determine the spatial selection function requires understanding how distances relate to dereddened H_0 magnitudes and what the extinction is as a function of distance for a given line of sight. To get a sense of how the MW spatial volume is sampled by the RC sample of stars described in this paper, we show the selection function as a function of position in Figure 12, assuming a RC absolute H-band magnitude of -1.49 (Laney et al. 2012), and using the median A_H for the stars in the statistical sample in each line of sight (in reality, the extinction will be less closer to the Sun and greater at the faint end, so the spatial sampling will cover a slightly smaller range than shown here). This figure demonstrates that the statistical subsample of the RC sample presented in this paper provides a large-scale sampling of the MW volume near the disk that is useful for statistical analyses of the distribution of elemental abundances in the Milky Way disk.

5. ASTROPHYSICAL SAMPLING WITH THE RED CLUMP

The second ingredient for relating the observed spectroscopic sample of stars to the underlying Galactic stellar populations is to determine how the spectroscopic tracer—RC stars in our case—relates to the full population. The RC stage in the evolution of stars with metallicities around solar is a relatively short phase for stars with masses of approximately 1 to 2 $M_\odot$ lasting for about 100 Myr. As such, the chance of finding stars in this stage of stellar evolution is small compared to the total lifetime of the stars, and only a small fraction of stars of a given age and metallicity will at any given time find themselves within the RC bounds given in Section 2. However, the RC is a relatively long phase compared to other evolved stages and in that respect the RC is perhaps the best population tracer among giants. In this section, we use the PARSEC stellar isochrone models to determine the properties of stars in our RC selection region and how they relate to the full stellar population.

Overall, the RC selection defined in this paper excludes stars with (1) metallicities $\lesssim -1$ and (2) ages $\lesssim 800$ Myr. These are primarily due to the APOGEE color cut and the subsequent cuts in Equations (6), (7), and (8). APOGEE's blue $(J-K_s)_0 \geqslant 0.5$ cut excludes RC stars with low metallicities: Equation (6) evaluated at $(J-K_s)_0 = 0.5$ gives a lower limit for the metallicity of ≈ -0.9. The additional blue cut in Equations (7) eliminates secondary red-clump stars with ages $\lesssim 1$ Gyr. Therefore, the RC selection in this paper selects intermediate-age and old stars in the MW disk.

Figure 13 shows the average initial mass of a star in the RC selection region defined in Section 2 as a function of age and metallicity. The typical mass is relatively constant as a function of metallicity and is smaller for larger ages. For a constant SFH, the average mass is $\approx 1.3\,M_\odot$ for near-solar metallicities and declines to about $1.2\,M_\odot$ at [Fe/H] ≈ -1. However, the average mass is sensitive to the SFH: For an exponentially declining SFH with an e-folding time of 8 Gyr, starting at 10 Gyr, the average mass is $\approx 0.1\,M_\odot$ lower than that for a constant SFH for all metallicities. For an old population of stars, the average mass

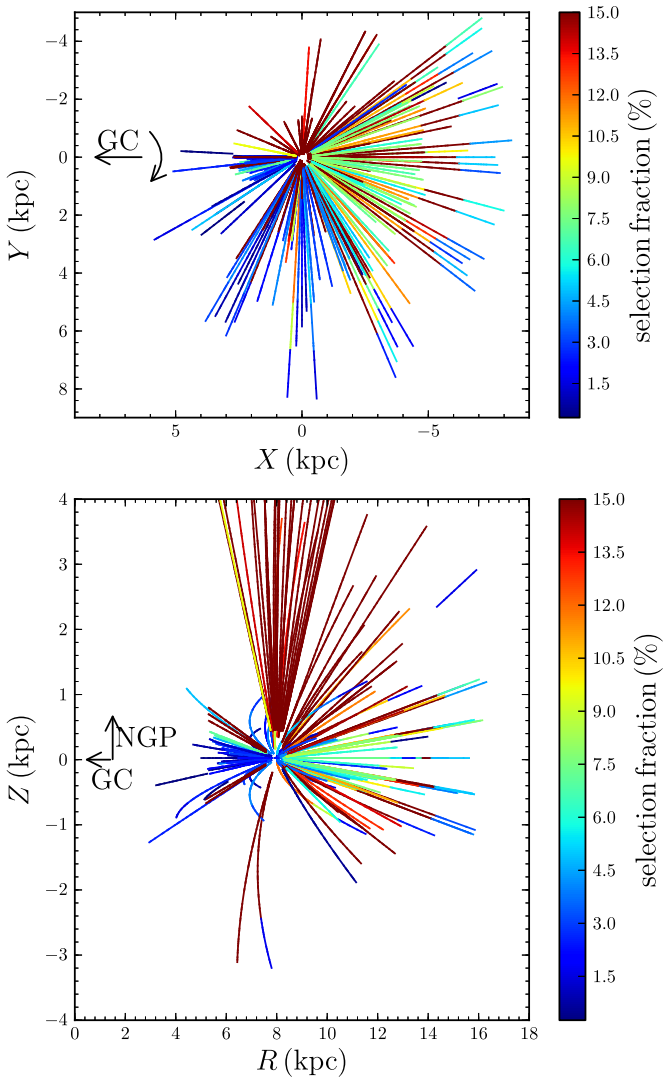

Figure 12. APOGEE selection function, i.e., the fraction of all potential targets observed spectroscopically and present in the statistical sample. The selection function, which intrinsically is a function of (l, b, H), is illustrated here as a function of Galactic coordinates X and Y (top panel) and of Galactocentric radius R and Z (bottom panel). H-band magnitudes are converted into distances using an absolute magnitude of -1.49 (Laney et al. 2012) and the median extinction in each field. Some high-latitude fields have selection fractions up to 95% and are saturated in the color scale employed in this figure. Low latitude ($|b| < 10^\circ$) fields at the same Galactic longitude have been dithered by 2° in the top panel for display purposes. The completeness is low near the Galactic midplane and toward the Galactic center.

(A color version of this figure is available in the online journal.)

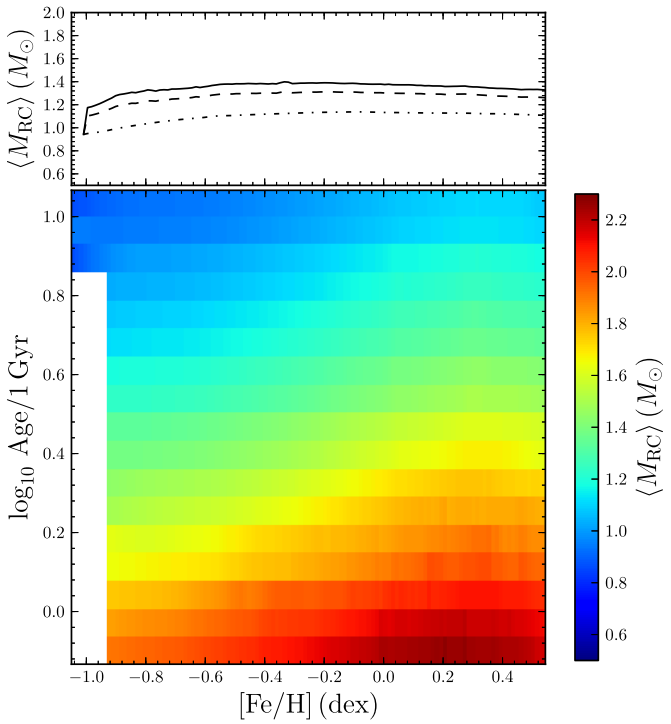

Figure 13. Average initial mass of a star in the RC selection region defined in Section 2 as a function of age and metallicity Z. The top panel shows the average mass integrated over a constant star formation rate (solid line) and exponentially declining star-formation histories with e-folding times of 8 Gyr (dashed line) and 1 Gyr (dash-dotted line).

(A color version of this figure is available in the online journal.)

drops to $\approx 1.0\,M_\odot$. The average mass can therefore change by about 30% depending on the SFH.

Because the RC stage (roughly the phase of core Helium burning, but our considerations in this section are purely based on the selection criteria from Section 2) is relatively short ($\approx 10^8$ yr), the fraction of stars of a single-burst stellar population (assuming here a lognormal Chabrier 2001 IMF) contained in the RC selection region is small. The relative fraction of the mass of a single-burst stellar population contained in the RC, as a function of age and metallicity, is shown in the top panel of Figure 14. Stars in the RC region are typically between one and four Gyr old (see Figure 15 below) and the relative mass fraction for ages above one Gyr is about 10^{-4}, a small fraction of the stellar population's mass. Similarly, the bottom panel of Figure 14 displays the fraction of the total mass each star in the RC region represents (this is equal to Figure 13 divided by the top panel). The dependence on age and metallicity is similar to that of the relative mass fraction. Integrating over a constant or exponentially declining SFH, these mass fractions are approximately constant with metallicity, but depend at the 25%–50% level on the SFH, as old populations contain relatively less of a stellar population's mass in the RC region than younger populations.

The varying mass fractions in Figure 14 imply that the RC as defined in this paper does not randomly sample the underlying age distribution of stars, but is instead typically skewed toward younger ages (see also Girardi & Salaris 2001). Figure 15 displays the relative probability, as a function of age, for stars in a stellar population that are present in the RC region. We calculate this probability using a metallicity distribution similar to that in the solar neighborhood (that of Casagrande et al. 2011, using the representation described in Section 3) and it can be approximated by the following functional form:

$$\begin{aligned}\ln f(a) &= -1.6314 + 3.8230a + 2.2133a^2 - 35.7414a^3 \\ &\quad (-0.1 \leqslant a \leqslant 0.23), \\ &= -1.0666 + 1.8664a - 9.0617a^2 + 4.5860a^3 \\ &\quad (a > 0.23), \\ &\quad \text{where } a = \log_{10}[\text{Age}/1\ \text{Gyr}]. \end{aligned} \tag{11}$$

Relative to a constant age distribution, the RC selection biases the sample to stars with ages between 1 and 4 Gyr. We sample all ages in the disk older than this, but the distribution is cut off below about 800 Myr. This effect is in large part due to our

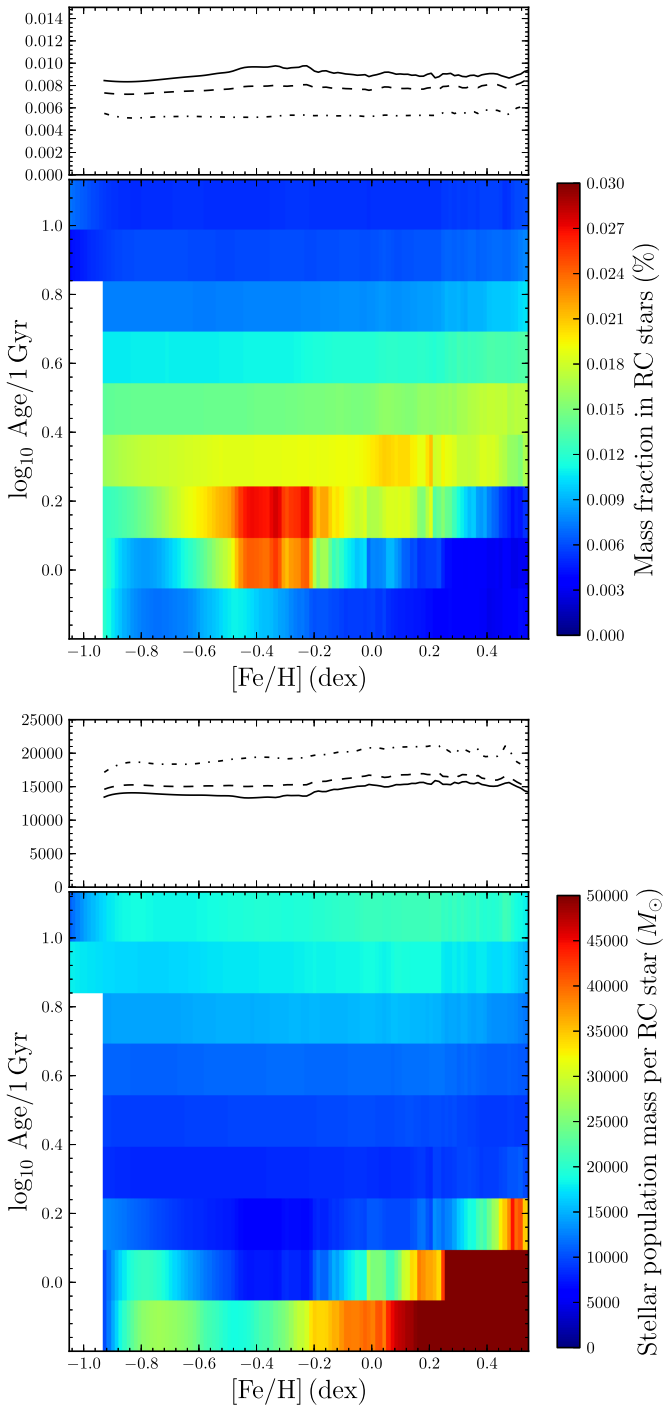

Figure 14. Sampling of the underlying stellar population of the RC selection region of Section 2. The top figure displays the fraction of the mass of a population contained in the RC region and the bottom figure shows the amount of total-stellar-population mass each RC star represents. The top panel in each figure show these fractions and masses averaged over the different star-formation histories discussed in the caption of Figure 13. Typically, the RC region contains about 0.01% of the mass of a stellar population and each RC star represents about 15,000 $M_\odot$.

(A color version of this figure is available in the online journal.)

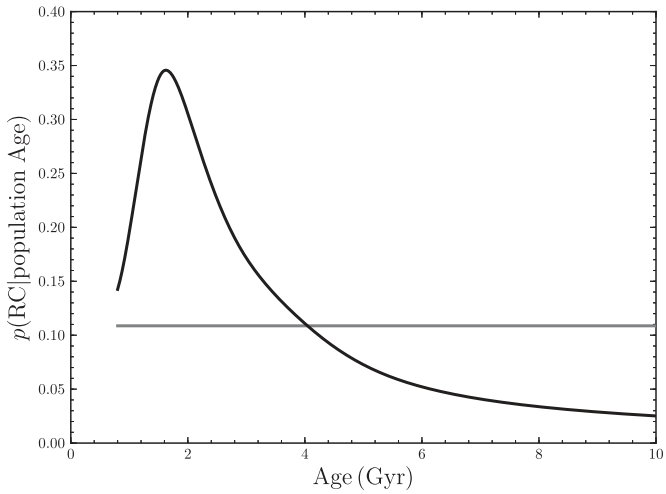

Figure 15. Relative probability for stars in a stellar population to be present in the RC region as a function of age. For a flat SFH, this is equivalent to the age distribution for stars in the RC region; other SFHs need to be multiplied with this function to obtain the age distribution of the RC. We have assumed a solar-neighborhood metallicity distribution (Casagrande et al. 2011; see Section 3). An approximate functional form for the age distribution is given in Equation (11). Relative to a uniform age distribution (gray line) the RC is heavily weighted toward stars with ages between 1 and 4 Gyr.

selection cuts: our color–metallicity cuts in Section 2 exclude the bluest, youngest red-clump stars at a given metallicity, because their luminosity distribution is not sufficiently narrow to allow precise distances to be assigned for these stars. This is also the reason that the red-clump age distribution derived by Girardi & Salaris (2001) peaks at lower ages and extends to younger red clump stars; they considered the full red clump, whereas we only consider the part of the RC that is narrow in luminosity and which is typically older.

The discussion in this section is based on PARSEC stellar-evolution models with mass loss on the giant branch modeled using the Reimers law with an efficiency parameter of $\eta = 0.2$ (see Section 2.2). While mass loss affects a star's mass during the RC phase, it neither influences the luminosity (see Section 2.2) nor the lifetime of the RGB and RC phases. Therefore, mass loss does not have any effect on how the RC samples the underlying stellar population. We have explicitly checked this by computing the total-stellar-population mass every RC star represents (bottom panel of Figure 14) and the age sampling (Figure 15) for PARSEC models with mass-loss efficiency parameters $\eta = 0.1$, 0.2, 0.3, and 0.4. We find small differences and in particular the age sampling of the RC is robust with respect to changes in η.

From the discussion in this section, it is clear that great care must be taken when using the RC as a spectroscopic tracer of the Galactic stellar distribution function, because the fraction of a stellar population's mass contained in the RC region and the manner in which other properties are sampled depends on the SFH—or, equivalently, the age distribution. This is unavoidable when using evolved rather than main-sequence stars as stellar population tracers; as discussed at the start of this section, the RC is a relatively long phase in the evolution of post-main-sequence stars and is therefore among the best population tracers among giants stars. The fact that the relation between the RC region and the full stellar population does not strongly depend on metallicity for a given SFH, combined with the fact that there is only a weak correlation observed in the solar neighborhood between age and metallicity (Edvardsson et al. 1993; Nordström et al. 2004), means that the RC sampling of the metallicity distribution of stellar populations older than 1 Gyr should be relatively uniform. However, age is not sampled uniformly (see Figure 15) and the detailed distribution of elemental abundances

likely depends strongly on age, such that detailed studies need to take the likely age distribution of the RC sample into account.

6. THE APOGEE-RC CATALOG

In this section, we discuss the construction of the APOGEE-RC catalog from the superset of data to be released as part of SDSS-III's DR11 and the contents of the catalog. We also briefly consider sources of proper motions for the catalog stars. Because SDSS-III has a yearly data release schedule, we do not release the APOGEE-RC catalog with this paper; it will instead be part of the SDSS-III DR11, currently scheduled for 2014 December. At the time of writing this 2014 December release is planned to also contain the full three-year APOGEE data as part of DR12. For public use, the DR11 APOGEE-RC catalog will therefore immediately be made obsolete by the DR12 APOGEE-RC catalog. Full details on how to obtain the APOGEE-RC catalog and what it contains will be given in the DR11/DR12 documentation.

6.1. Catalog Creation

The starting point is the catalog of all unique stars observed spectroscopically, and to be released as part of DR11. For these stars, we calculate extinction-corrected 2MASS JHK_s magnitudes, using the extinction corrections derived by the RJCE method (Majewski et al. 2011) for APOGEE stars (we use the extinction corrections calculated prior to target selection, for consistency). We then employ the calibrated metallicities and surface gravities using the corrections of Mészáros et al. (2013) and convert the metallicity [Fe/H] to metal mass fraction Z assuming $Z_\odot = 0.017$ and solar abundance ratios. The dereddened color $(J-K_s)_0$, $\log g$, $T_{\rm eff}$ and metallicity Z are then used to select RC stars using the cuts described in Section 2. We also apply the additional $\log g$–$T_{\rm eff}$ cut of Equation (9). Stars selected in this way constitute the full DR11 APOGEE red-clump (APOGEE-RC) catalog. This sample consists of 10,341 stars.

The absolute K_s-band magnitudes for all of the RC stars are calculated using the model for M_{K_s} shown in the top panel of Figure 3, corrected for the calibration offset determined in Section 3. Using the selection function from Section 4, we also determine which RC stars are part of the statistical sample.

6.2. Catalog Contents

The APOGEE-RC catalog contains all of the basic data derived from the APOGEE spectra, such as the line-of-sight velocity, $T_{\rm eff}$, $\log g$, [Fe/H], as well as other abundances measured from the spectra. We also include photometry from 2MASS, extinction corrections, APOGEE targeting information, pipeline flags, and APOGEE identifiers to allow the objects in the APOGEE-RC catalog to be matched to the full APOGEE catalog. Full high-resolution spectra can be obtained from the SDSS-III database by using the APOGEE identifiers. We include distances derived from the absolute K_s magnitudes and, for convenience, we add Galactocentric coordinates calculated assuming $R_0 = 8$ kpc and $Z_0 = 25$ pc.

The distance distribution of the APOGEE-RC sample is presented in Figure 7. The distribution of the sample in the volume around the Sun and in Galactocentric coordinates is shown in Figure 8. These distributions demonstrate that the sample is dominated by disk stars at $|Z| \lesssim 1$ kpc, but the sample also contains some stars in the stellar halo. Because the RC is faint relative to more luminous red-giant APOGEE targets and as bulge fields are typically limited to $H \leqslant 11$ or $H \leqslant 12.2$, there are relatively few bulge stars contained in this sample.

6.3. Proper Motions

We have added matches to the UCAC-4 (Zacharias et al. 2013) and PPMXL (Roeser et al. 2010) proper-motion catalogs. However, the usefulness of these catalogs, which have proper motions uncertainties $\gtrsim 2$ mas yr^{-1} (both statistical and systematic), for the APOGEE-RC sample is extremely limited. Stars in the APOGEE-RC catalog have typical distances of a few kiloparsecs (see Figure 7). At these distances and farther, Galactic rotation typically leads to proper motions of ≈ 2 mas yr^{-1}, while random motions—≈ 30 km s^{-1} and smaller at larger distances from the Galactic center—lead to proper motions of about 6 mas yr^{-1} kpc. Therefore, at a few kiloparsecs the proper motion uncertainties are similar or greater than the intrinsic proper motions and the systematic uncertainties in these proper motion catalogs make extracting proper motions signals out of the noise difficult.

The *Gaia* astrometric space mission, launched on 2013 December 19, will measure proper motions with precisions better than 200 μas yr^{-1} for all stars with *Gaia* $G \leqslant 20$ over its five-year mission. As G is a white-light optical bandpass it is much more strongly affected by dust extinction than the infrared APOGEE observations ($A_G/A_H \approx 4$). We estimate the *Gaia* G-band magnitudes of stars in the APOGEE-RC sample by using the PARSEC isochrones in the SDSS and 2MASS passbands in the RC region defined in Section 2 and using the transformation between g, $g-z$ and G of Table 5 of Jordi et al. (2010). We calculate $V - I_{\rm C}$ from $g - i$ as

$$V - I_{\rm C} = 0.675\,(g-i) + 0.364 \ \text{ if } g - i \leqslant 2.1 \quad (12)$$

$$V - I_{\rm C} = 1.110\,(g-i) - 0.520 \ \text{ if } g - i > 2.1, \quad (13)$$

inspired by the data of Jordi et al. (2010). For a given extinction A_H we calculate the extinction in the *Gaia* band using the highest extinction entry in Table 8 of Jordi et al. (2010) and assuming $A_H/A_V = 0.18307$. We then use the projected astrometric performance as a function of $(G, V - I_{\rm C})$ from the *Gaia* Performance Web site[44] to calculate the proper-motion precision. The resulting expected precision in the transverse motion based on the *Gaia* proper motions at different apparent magnitudes and for different amounts of extinction is shown in Figure 16. These precisions only include the effect of the proper motion uncertainty; additional uncertainty comes from the 5%–10% RC distance uncertainty. The variation at a given magnitude in this figure is due to the spread in G and $V - I_{\rm C}$ in the RC region for a given magnitude.

Figure 16 shows that, even at large extinctions, most stars in the APOGEE-RC catalog will be bright enough to have *Gaia* proper motions, with only the faintest and most heavily extincted stars falling below the $G = 20$ *Gaia* magnitude limit. Therefore, *Gaia* will provide highly precise proper motions for the vast majority of our sample, leading to errors in the transverse velocity $\lesssim 5$ km s^{-1}. At the time of writing, *Gaia* is expected to release preliminary proper motions 28 months after launch using 20 months of data. The proper motion uncertainties in that first data release are expected to be worse by a factor of

[44] Available at http://www.rssd.esa.int/index.php?page=Science_Performance&project=GAIA.

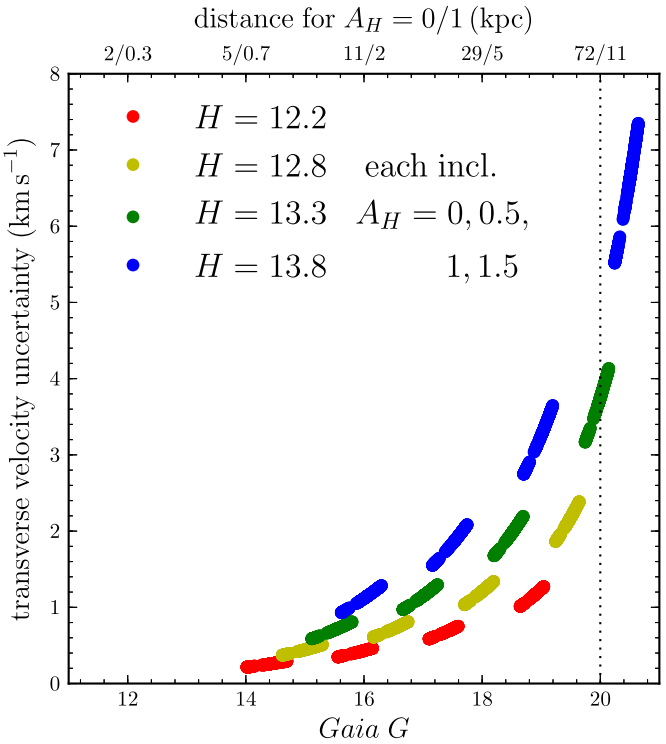

Figure 16. Expected transverse velocity precision of *Gaia* for stars in the APOGEE-RC sample at different apparent magnitudes (colors) and different amounts of extinction (four bands for each color of increasing G magnitude). The precisions only include the uncertainty arising from the proper motion, not that produced by the 5%–10% RC distance uncertainty. These are end-of-mission precisions; the first *Gaia* data release at launch+28 months with one third of the data will have proper motion uncertainties that are $\approx 3\sqrt{3} \approx 5$ times larger. The top axis shows approximate distances computed assuming $M_G^{\rm RC} = 0.71$ ($G - H \approx 2.2$ for the RC); ≈90% of stars in the DR11 RC catalog have $A_H < 0.5$, with a median A_H of 0.2. The vast majority of stars in the APOGEE-RC sample will have precise proper motions out to 10 kpc from *Gaia*, even in regions of high extinction.

(A color version of this figure is available in the online journal.)

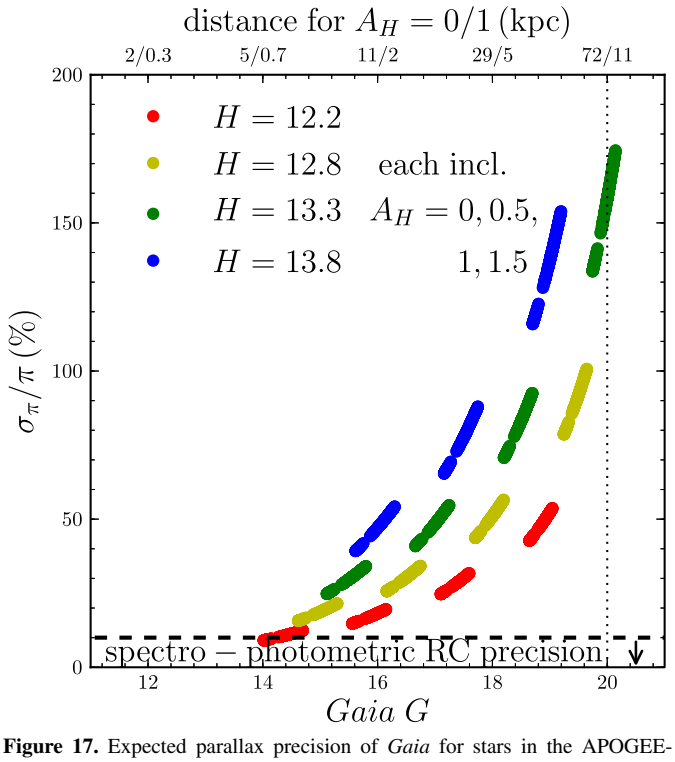

Figure 17. Expected parallax precision of *Gaia* for stars in the APOGEE-RC sample at different apparent magnitudes (colors) and different amounts of extinction (four bands for each color of increasing G magnitude). These precisions are for the full five-year mission; the first *Gaia* data release at launch+28 months will have uncertainties that are $\approx\sqrt{3} \approx 1.7$ times larger. The spectro-photometric RC distances are more precise than the *Gaia* parallaxes for all but the brightest stars. At low extinction, the *Gaia* parallaxes can identify RGB contamination in the RC sample.

(A color version of this figure is available in the online journal.)

≈5 ($[20/60]^{-3/2}$). Even with these larger uncertainties, most stars in the APOGEE-RC sample will have sub-mas yr^{-1} proper motions and most will have uncertainties below 250 μas yr^{-1}, or 10 km s^{-1}.

In Figure 17, we display the expected *Gaia* relative parallax precision for stars in the APOGEE-RC catalog, computed in a similar way as the proper motion uncertainties above (the expected end-of-mission proper motion uncertainties are half the expected parallax uncertainties). The parallaxes that will be available in the launch+28 months release will have uncertainties that are larger by a factor of ≈1.7 ($[20/60]^{-1/2}$). The spectro-photometric RC distances computed in Sections 2 and 3 are more precise than the *Gaia* parallaxes for all but the brightest stars that do not suffer from much extinction; these bright RC stars will be highly informative for an improved calibration of the RC distances. However, for many RC candidates, the *Gaia* parallaxes could distinguish between true RC stars or RGB interlopers by comparing the spectro-photometric distance to the parallax.

7. AZIMUTHAL METALLICITY VARIATIONS IN THE MILKY WAY MIDPLANE

The RC catalog with high-resolution abundances and very accurate distances will allow the distribution of abundances in the MW's disk to be mapped in unprecedented detail. As an illustration of this capability, we discuss in this section spatial variations in the median metallicity close to the midplane of the MW's disk. Because there is a strong radial metallicity gradient for the intermediate-age stars in the RC catalog (see below), the average metallicity can be used as a tracer of the orbits of stars with different mean orbital radii. For example, if closed orbits in the MW disk are non-circular (e.g., elliptical as discussed below), then the azimuthal dependence of the radius of a closed orbit maps into an azimuthal dependence of the average [Fe/H]. Non-steady-state non-axisymmetric flows, such as those induced by growth of the Galactic bar or transient spiral structure, can also be traced by azimuthal [Fe/H] variations because the inhomogeneities in the [Fe/H] distribution induced by these perturbations will remain visible for multiple dynamical times. As a specific example, recent simulations of the evolution of galactic disks (Di Matteo et al. 2013) have shown that for galaxies with a radial metallicity gradient, the presence (or absence) of azimuthal metallicity variations in the stars can constrain recent radial mixing induced by the bar. Mixing induced by transient spiral structure (Sellwood & Binney 2002) would lead to smaller, but similar effects. Such mixing would induce azimuthal [Fe/H] variations of comparable magnitude to the radial variations that last for $\gtrsim$1 Gyr.

We start by showing the radial midplane metallicity gradient in Figure 18, specifically the median metallicity as a function of Galactocentric radius for all stars in the RC catalog contained within 50 pc from the midplane. The data can be well fit by a single linear relation (except for a discrepant point at $R \approx 12$ kpc) with a slope of -0.09 ± 0.01 dex kpc^{-1} and a

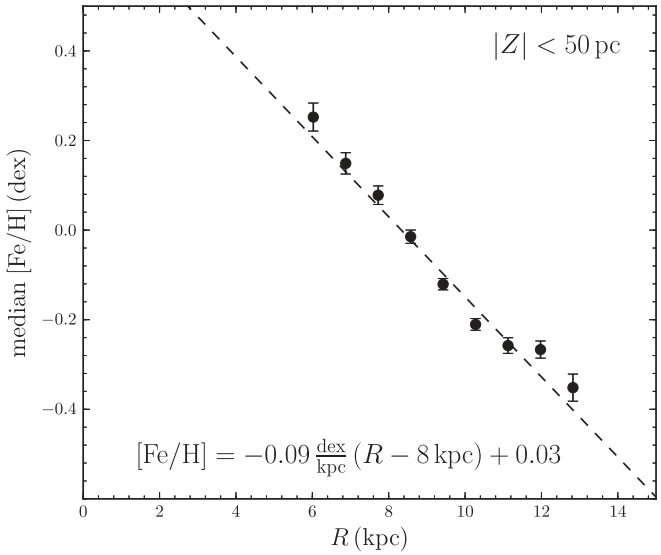

Figure 18. Radial metallicity gradient in the midplane of the Milky Way (heights <50 pc) from 971 stars near the midplane in the DR11 APOGEE-RC sample. The uncertainties in the slope and zero-point are both 0.01 dex. The metallicity gradient of stars that are a few Gyrs old is quite steep in the midplane.

local normalization at $R_0 = 8$ kpc of 0.03 ± 0.01 dex. Thus, the median metallicity in the solar neighborhood is approximately solar and the metallicity gradient is quite steep for stars that are typically between 1 and 5 Gyr old (see Section 5). This measurement agrees with previous determinations of the metallicity gradient of intermediate-age stars (see Nordström et al. 2004; Hayden et al. 2014, and references therein) and open clusters older than ≈1 Gyr (e.g., Yong et al. 2012; Frinchaboy et al. 2013).

The RC catalog covers a region around the Sun that spans about 45° in Galactocentric azimuth ϕ, allowing the mapping of the median metallicity in both R and ϕ. We extend the range in vertical heights to include all stars in the RC catalog within 250 pc from the midplane such that we can use small pixels in R and ϕ, as allowed by our precise distances. Figure 19 presents the two-dimensional behavior of the median metallicity in rectangular coordinates. Figure 20 shows the azimuthal metallicity residuals with respect to the median metallicity at each radius in cylindrical coordinates. The typical uncertainty in the median metallicity of a given two-dimensional spatial pixel is about 0.02 dex. The residual map in Figure 20 clearly demonstrates that there are no significant azimuthal variations within the observed octant above the uncertainty of 0.02 dex; deviations that are present have a standard deviation of 0.02 dex. Remarkably, this constraint is more than an order of magnitude tighter than the radial variation of the metallicity (Figure 18). This is the first time that azimuthal variations in the metallicity distribution of intermediate-age stars have been constrained. Previous investigations of azimuthal gradients in the abundance distribution of young tracers of the disk (ages $\lesssim$1 Gyr) have obtained mixed results, with some studies seeing variations (Davies et al. 2009), while others do not (Luck & Lambert 2011). Because young tracers have ages that are not much larger than the rotational period ($T_\phi \approx 250$ Myr; see below), their azimuthal distribution likely more strongly reflects their birth properties than dynamical stellar mixing. The opposite is the case for the RC stars that we use, which are all older than 1 Gyr $\approx 4\,T_\phi$ and are typically 2 Gyr $= 8\,T_\phi$ (Figure 15).

The absence of significant variations in the median metallicity with Galactocentric azimuth limits the extent to which closed

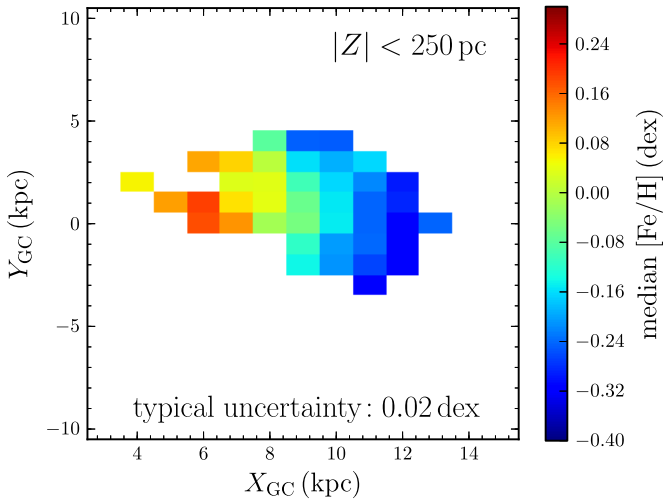

Figure 19. Two-dimensional distribution of the median metallicity near the midplane (heights <250 pc) from 4,330 stars in the DR11 APOGEE-RC sample. This figure shows a map of the median metallicity in rectangular coordinates.

(A color version of this figure is available in the online journal.)

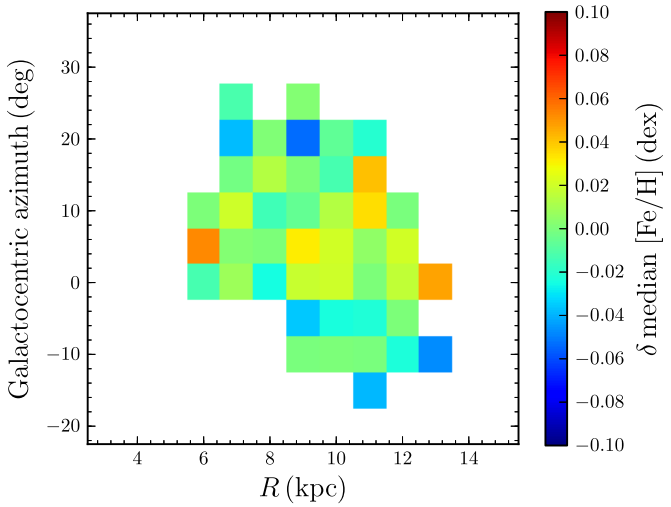

Figure 20. Absence of azimuthal metallicity variations in the Milky Way disk. This figure shows the azimuthal variation of the median metallicity (with respect to the median for each radius, see Figure 18) in cylindrical coordinates. There are no azimuthal variations in the ≈45° region near the Sun to within the uncertainties of ≈0.02 dex.

(A color version of this figure is available in the online journal.)

orbits in the Galactic disk are non-circular. As an example we consider that the MW disk is elliptical due to a $m = 2$ perturbation $\Delta\Phi = \varepsilon_\Psi V_c^2/2 \cos 2\,(\phi - \phi_b)$ to the potential Φ_0 where ε_Ψ is the dimensionless amplitude of the perturbation, V_c is the circular velocity, and ϕ_b is a position angle (Kuijken & Tremaine 1994); we assume that the unperturbed circular velocity curve is flat, i.e., $\Phi_0 \propto \ln R$. The ellipticity of the equipotential surfaces and of the closed orbits is $\approx 1 - \varepsilon_\Psi$. Such ellipticity in the MW is only mildly constrained, especially if the Sun lies near the minor or major axis of the perturbation (Kuijken & Tremaine 1991, 1994), but ellipticities of ≈5% are common in external MW-like galaxies (Rix & Zaritsky 1995). If $\varepsilon_\Psi \approx 0.05$ in the MW, then there will be coherent non-circular flows with an amplitude of ≈ 10 km s^{-1} and estimates of the circular velocity could be impacted by similar amounts (Kuijken & Tremaine 1994).

Elliptical motions that lead to radial variations larger than 200 pc along closed orbits within the ≈45° azimuthal region

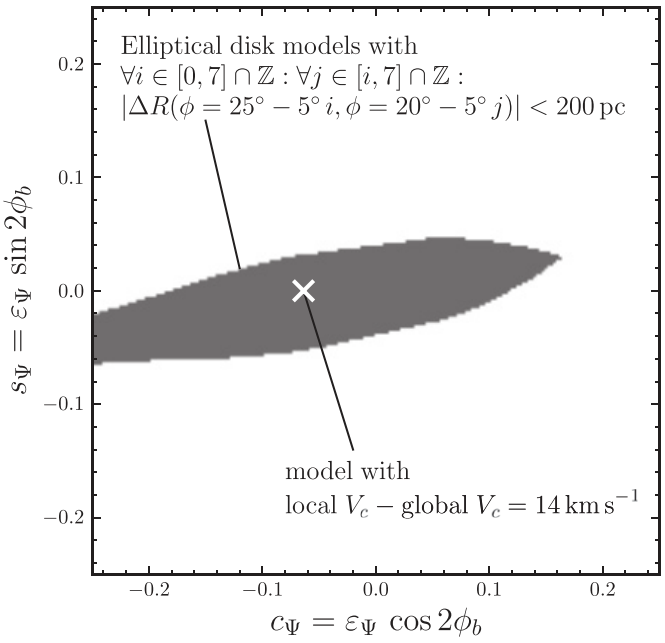

Figure 21. Constraints on the ellipticity of the MW's disk from the absence of azimuthal metallicity variations within a ≈45° region near the Sun. The ellipticity is induced by a static cos2ϕ perturbation to an axisymmetric, flat-rotation-curve background potential with equipotential surfaces with ellipticity $1-\varepsilon_\Psi$ and a position angle ϕ_b. The constraints are shown in terms of parameters c_Ψ and s_Ψ that describe perturbations that are symmetric and asymmetric, respectively, with respect to the Sun–Galactic center line. Ellipticity that leads to radial variations larger than 200 pc for closed orbits within the observed azimuthal range would induce azimuthal [Fe/H] variations $\gtrsim$0.02 dex and are therefore ruled out. Asymmetric ($|s_\Psi| \gtrsim 0.05$) and positive, symmetric ($c_\Psi \gtrsim 0.05$) are strongly constrained. Models in which the local standard of rest (LSR), i.e., the rotational velocity of the local closed orbit, is ahead of the axisymmetric circular velocity without an accompanying mean radial motion of the LSR ($c_\Psi < 0$, $s_\Psi \approx 0$) are allowed. An example of such a model is indicated by the ×.

near the Sun lead to $\gtrsim$0.02 dex azimuthal variations in the average metallicity. As we do not observe such variations, these closed orbits are disfavored by the data. Specifically, we consider any elliptical closed orbit that leads to $|\Delta R| > 200$ pc for any of the $|\Delta\phi|$ between 25° and −15° to be ruled out. We present these constraints in Figure 21. This figure uses an alternative parameterization of the elliptical disk potential where the perturbation is split into a component $c_\Psi = \varepsilon_\Psi \cos 2\phi_b$ that is symmetric with respect to the Sun–Galactic-center line and a component $s_\Psi = \varepsilon_\Psi \sin 2\phi_b$ that is asymmetric. Elliptical models where the Sun lies on the major or minor axis ($s_\Psi \approx 0$ and $c_\Psi > 0$ and <0, respectively) are much less constrained than models where the Sun is in between the major and minor axis ($c_\Psi \approx 0$). This is because for the latter models $R(\phi)$ is almost entirely monotonic with ϕ within the observed region, such that large $|\Delta R|$ occur; if the Sun lies near the major or minor axis, much smaller $|\Delta R|$ exist. Models where the Sun lies near the minor axis are the least constrained, with large $c_\Psi < 0$ allowed by the data. In such models the closed orbit at the Sun's position has a rotational velocity that is larger than the average, axisymmetric V_c by $|c_\Psi|\,V_c$; offsets up to 40 km s^{-1} are allowed by these data. In particular, a model where the closed orbit near the Sun is ahead of the average V_c by 14 km s^{-1} as proposed by Bovy et al. (2012a) to explain the APOGEE stellar kinematics in the disk, is allowed; this model is indicated in Figure 21 by a white cross. RC data from the final year of APOGEE combined with data from APOGEE-2 will extend the mapping of azimuthal [Fe/H] variations over at least $\phi = 45°$ to $\phi = -45°$. This mapping will allow limits on c_Ψ and s_Ψ that are $\lesssim$0.05.

If the MW's bar or spiral structure now or in the recent past had induced significant radial mixing of stars, this generically leads to azimuthal variations over similar spatial scales. The fact that we observe azimuthal metallicity variations to be smaller than the radial metallicity variation over ≈200 pc (the metallicity gradient is ≈0.1 dex kpc^{-1} or 0.02 dex (200 pc)$^{-1}$), indicates that no significant radial mixing over these spatial scales has recently occurred (see Di Matteo et al. 2013 for a detailed discussion of this in the context of mixing induced by a bar; see also the azimuthal variations in the density of migrating stars in Figure 10 in Roškar et al. 2012); specifically, $\lesssim$10% of stars can have migrated $\gtrsim$2 kpc with $\Delta\phi \approx 45°$ near the Sun. Any azimuthal variation will smooth out after the mixing ends. Because the MW's rotation curve is approximately flat in the region where we map the median metallicity (e.g., Gunn et al. 1979; Bovy et al. 2012a), $|d\Omega/dR| \approx \Omega/R$, such fluctuations over a scale ΔR across an azimuthal range $\Delta\phi$ near the Sun would disappear in approximately few × T_ϕ × $(\Delta\phi/360°)$ × $\left(R_0/\max(\Delta R, \sigma_{R_g})\right)$, where T_ϕ is the rotational period (≈250 Myr) and σ_{R_g} is the spread in guiding-star radii (≈0.1 R near R_0 or about 1 kpc for the intermediate-age disk; Bovy et al. 2012a). For fluctuations below 1 kpc over the 45° range probed by the DR11 APOGEE-RC catalog, this timescale is approximately a few times 250 Myr near the Sun and about 50% larger in the outer disk regions shown in Figure 20. Therefore, our constraints on mixing on kiloparsec scales apply to approximately the last Gyr of the MW's evolution. However, quantitative constraints on realistic migration scenarios will require more detailed modeling of the azimuthal signature of radial migration, its dissolution over time, and its observability within the APOGEE survey volume.

The absence of azimuthal variations in the median metallicity can also be used to constrain distance systematics. Any systematic distance offsets in the RC sample would induce azimuthal gradients in metallicity: such offsets would distort rings of stars at constant R onto a locus spanning a range of apparent $\tilde{R}$, with a strong correlation between $\tilde{R} - R$ and azimuth ϕ. The metallicity distribution of stars at a constant apparent $\tilde{R}$ would therefore show apparent azimuthal variations that correspond to the real radial variations. Changing all of the distances in the RC catalog by 50% upward or downward induces clear azimuthal variations at large and small R, respectively. Assuming that there are no intrinsic azimuthal variations, this result excludes such large distance systematics. Smaller distance systematics induce smaller azimuthal gradients, and azimuthal variations over the volume probed by the RC catalog are minimized for distance systematics within a few percent of the distances that we assigned in Section 3 (using the maximum of the median absolute azimuthal deviations δ[Fe/H] in $\Delta R = 1$ kpc bins to quantify the accuracy of the distances). Thus, we conclude from this test that the distances in the RC catalog are accurate to a few percent, in agreement with the considerations in Section 3. Because contamination by RGB stars at significantly different distances (typical differences of ∼70%) would lead to distance systematics, this test also indicates that the overall RGB contamination must be $\lesssim$5%, in accordance with the direct contamination estimates using asteroseismic evolutionary-state classifications in Section 2.

8. CONCLUSION

We have presented a new method for selecting individual likely RC stars from spectro-photometric data. This approach was used to produce a sample of RC stars with high purity from the APOGEE data set. The selection technique is a combination of simple cuts in ($\log g$, $T_{\rm eff}$, [Fe/H], $[J-K_s]_0$) motivated using stellar isochrone models and calibrated using high-quality seismic $\log g$ data from a subsample of APOGEE stars with measured oscillation frequencies from *Kepler*. These cuts in particular select RC stars for which the intrinsic absolute-magnitude distribution is very narrow ($\sigma \lesssim 0.1$ mag), such that highly precise distances for these stars can be obtained. Tests using *Kepler* stars for which the evolutionary state was measured from their photometric variability show that the purity of the sample is $\gtrsim$93%. Using stellar isochrone models we calculate the small ($\lesssim$5%) deviations from a standard candle RC magnitude and we calibrate the distances against RC stars in *Hipparcos*. This procedure results in distances that are unbiased to within ≈2% and have random uncertainties of ≈5%.

We produce the APOGEE-RC catalog using the new RC selection method and distance calculation. This catalog is currently based on SDSS DR11, and contains 10,341 stars with accurate and precise distances, stellar parameters, and elemental abundances. The catalog will be released publicly as part of the public combined DR11/DR12 data release (currently scheduled for 2014 December); full details on the contents of the catalog will be given in the documentation accompanying this data release. Future data releases of SDSS-IV will expand the current RC catalog and the data it contains.

The APOGEE target selection and the subsequent RC selection introduces biases in the way the underlying stellar populations are represented in the sample. These biases are important for many detailed investigations of the abundance structure of the disk and need to be corrected for. As discussed in Section 4, we have determined the manner in which stars in the RC catalog were selected from the underlying 2MASS photometry for a subsample of stars for which this is possible. Selection weights for this statistical sample are included in the catalog and code that evaluates the selection function will be made publicly available with the release of the catalog. Beyond this first bias are the astrophysical selection effects due to the fact that RC stars as any other kind of giants are an age- and metallicity-biased tracer of the underlying populations. These effects are discussed in detail in Section 5. The main conclusion from this analysis are that the biases are relatively constant with metallicity for a given star-formation history, but they depend at the 25% level on the star-formation history.

The RC catalog will be useful for exploring the full stellar distribution function of spatial location, kinematics, and abundances in the MW disk, because of the large volume covered by the data, the precise distances permitting study of the smooth structure and any substructure to be resolved, and the availability of a large number of elemental abundances from the high-resolution APOGEE spectra. In Section 6.3, we showed that *Gaia* will soon provide highly precise proper motions for the vast majority of stars in the RC catalog, giving transverse velocities precise to $<5\,{\rm km\,s^{-1}}$ over the volume covered by the RC catalog, while the photometric RC distances will remain more precise than the *Gaia* parallaxes. This information, combined with the excellent APOGEE line-of-sight velocities with uncertainties $\lesssim 0.1\,{\rm km\,s^{-1}}$, will allow explorations of the kinematics in the MW disk that are not limited by velocity uncertainties. Currently, stellar parameters measured from the APOGEE spectra are limited to $T_{\rm eff}$, $\log g$, [Fe/H], and $[\alpha/{\rm Fe}]$, but these already lead to qualitatively new constraints on the abundance distribution in the MW's disk. In Section 7 we used the current RC catalog to make the first map of the azimuthal metallicity distribution of stars of a few Gyrs old and we limit azimuthal variations of the median metallicity to be $\lesssim$0.02 dex. This result limits the overall ellipticity of the MW disk and the amount of large-scale stellar radial mixing within the last Gyr. In D. Nidever et al. (in preparation), we explore the distribution of ([Fe/H],$[\alpha/{\rm Fe}]$) over $5\,{\rm kpc} < R < 12\,{\rm kpc}$ and $|Z| < 2\,{\rm kpc}$ with the large data set of RC stars, which allows strong, novel constraints on the chemical evolution of the MW's disk.

It is a pleasure to thank Friedrich Anders, Victor Debattista, Rok Roškar, Martin Smith, and Scott Tremaine for helpful comments and discussions. J.B. was supported by NASA through Hubble Fellowship grant HST-HF-51285.01 from the Space Telescope Science Institute, which is operated by the Association of Universities for Research in Astronomy, Incorporated, under NASA contract NAS5-26555. J.B. also gratefully acknowledges the hospitality of the Asia Pacific Center for Theoretical Physics (APCTP) during the 7th Korean Astrophysics Workshop, where parts of this research were performed. D.L.N. was supported by a McLaughlin Fellowship at the University of Michigan. H.W.R. has been supported by the European Research Council under the European Union's Seventh Framework Programme (FP 7) ERC grant agreement No. [321035]. P.M.F. was supported by a NSF AST-1311835 grant. T.S.R. has been supported by CNPq-Brazil scholarship. S.B. acknowledges partial support from NSF grant AST-1105930 and NASA grant NNX13AE70G. T.C.B. acknowledges partial support from grant PHY 08-22648: Physics Frontier Center/Joint Institute for Nuclear Astrophysics (JINA), awarded by the U.S. National Science Foundation. W.J.C. and Y.E. acknowledge the support of the UK Science and Technology Facilities Council (STFC). Funding for the Stellar Astrophysics Centre is provided by The Danish National Research Foundation (grant agreement No.: DNRF106). D.A.G.H. and O.Z. acknowledge support provided by the Spanish Ministry of Economy and Competitiveness under grant AYA-2011-27754. The research leading to the presented results has received funding from the European Research Council under the European Community's Seventh Framework Programme (FP7/2007-2013)/ERC grant agreement No. 338251 (StellarAges) and from the Deutsche Forschungsgemeinschaft (DFG) under grant SFB 963/1 "Astrophysical flow instabilities and turbulence." The research is supported by the ASTERISK project (ASTERoseismic Investigations with SONG and Kepler) funded by the European Research Council (grant agreement No.: 267864). A.S. is partially supported by the MICINN grant AYA2011-24704.

Funding for SDSS-III has been provided by the Alfred P. Sloan Foundation, the Participating Institutions, the National Science Foundation, and the U.S. Department of Energy Office of Science. The SDSS-III Web site is http://www.sdss3.org/.

SDSS-III is managed by the Astrophysical Research Consortium for the Participating Institutions of the SDSS-III Collaboration including the University of Arizona, the Brazilian Participation Group, Brookhaven National Laboratory, Carnegie Mellon University, University of Florida, the French Participation Group, the German Participation Group, Harvard University, the Instituto de Astrofisica de Canarias, the Michigan State/Notre Dame/JINA Participation Group, Johns Hopkins

University, Lawrence Berkeley National Laboratory, Max Planck Institute for Astrophysics, Max Planck Institute for Extraterrestrial Physics, New Mexico State University, New York University, Ohio State University, Pennsylvania State University, University of Portsmouth, Princeton University, the Spanish Participation Group, University of Tokyo, University of Utah, Vanderbilt University, University of Virginia, University of Washington, and Yale University.

REFERENCES

Alvarez, R., & Plez, B. 1998, A&A, 330, 1109
Alves, D. R. 2000, ApJ, 539, 732
Anders, F., Chiappini, C., Santiago, B. X., et al. 2014, A&A, 564, A115
Bedding, T. R., Mosser, B., Huber, D., et al. 2011, Natur, 471, 608
Bessell, M. S., & Brett, J. M. 1988, PASP, 100, 1134
Binney, J., Burnett, B., Kordopatis, G., et al. 2014, MNRAS, 437, 351
Bonatto, C., Bica, E., & Girardi, L. 2004, A&A, 415, 571
Bovy, J., Allende Prieto, C., Beers, T. C., et al. 2012a, ApJ, 759, 131
Bovy, J., Hogg, D. W., & Rix, H.-W. 2009, ApJ, 704, 1704
Bovy, J., & Rix, H.-W. 2013, ApJ, 779, 115
Bovy, J., Rix, H.-W., & Hogg, D. W. 2012b, ApJ, 751, 131
Bovy, J., Rix, H.-W., Hogg, D. W., et al. 2012c, ApJ, 755, 115
Bovy, J., Rix, H.-W., Liu, C., et al. 2012d, ApJ, 753, 148
Bressan, A., Marigo, P., Girardi, L., et al. 2012, MNRAS, 427, 127
Brown, T. M., Latham, D. W., Everett, M. E., & Esquerdo, G. A. 2011, AJ, 142, 112
Carpenter, J. M. 2001, AJ, 121, 2851
Casagrande, L., Schönrich, R., Asplund, M., et al. 2011, A&A, 530, 138
Casagrande, L., Silva Aguirre, V., Stello, D., et al. 2014, ApJ, 787, 110
Chabrier, G. 2001, ApJ, 554, 1274
Chen, B., Stoughton, C., Smith, J. A., et al. 2001, ApJ, 553, 184
Churchwell, E., Babler, B. L., Meade, M. R., et al. 2009, PASP, 121, 213
Davies, B., Origlia, L., Kudritzki, R.-P., et al. 2009, ApJ, 696, 2014
de Bruijne, J. H. J. 2012, Ap&SS, 341, 31
Di Matteo, P., Haywood, M., Combes, F., Semelin, B., & Snaith, O. N. 2013, A&A, 553, A102
Edvardsson, B., Andersen, J., Gustafsson, B., et al. 1993, A&A, 275, 101
Eisenstein, D., Weinberg, D. H., Agol, E., et al. 2011, AJ, 142, 72
ESA 1997, The Hipparcos and Tycho Catalogues (Noordwijk: ESA; ESA SP-1200)
Frinchaboy, P. M., Thompson, B., & Jackson, K. M. 2013, ApJL, 777, L1
Ghez, A. M., Salim, S., Weinberg, N. N., et al. 2008, ApJ, 689, 1044
Gillessen, S., Eisenhauer, F., Trippe, S., et al. 2009, ApJ, 692, 1075
Girardi, L. 1999, MNRAS, 308, 818
Girardi, L., Bressan, A., Bertelli, G., & Chiosi, C. 2000, A&AS, 141, 371
Girardi, L., & Salaris, M. 2001, MNRAS, 323, 109
Groenewegen, M. A. T. 2008, A&A, 488, 935
Gunn, J. E., Knapp, G. R., & Tremaine, S. D. 1979, AJ, 84, 1181
Gunn, J. E., Siegmund, W. A., Mannery, E. J., et al. 2006, AJ, 131, 2332
Gustafsson, B., Edvardsson, B., Eriksson, K., et al. 2008, A&A, 486, 951
Hayden, M. R., Holtzman, J. A., Bovy, J., et al. 2014, AJ, 147, 116
Hekker, S., Elsworth, Y., Mosser, B., et al. 2013, A&A, 556, A59
Jordi, C., Gebran, M., Carrasco, J. M., et al. 2010, A&A, 523, A48
Jurić, M., Ivezić, Ž., Brooks, A., et al. 2008, ApJ, 673, 864
Kaiser, N., Aussel, H., Burke, B. E., et al. 2002, Proc. SPIE, 4836, 154
Kallinger, T., Mosser, B., Hekker, S., et al. 2010, A&A, 522, 1
Keller, S. C., Schmidt, B. P., Bessell, M. S., et al. 2007, PASP, 24, 1
Koch, D. G., Borucki, W. J., Basri, G., et al. 2010, ApJ, 713, 79
Koesterke, L. 2009, in AIP Conf. Ser. 1171, Recent Directions in Astrophysical Quantitative Spectroscopy and Radiation Hydrodynamics, ed. I. Hubeny et al. (Melville, NY: AIP), 73
Koesterke, L., Allende Prieto, C., & Lambert, D. L. 2008, ApJ, 680, 764
Kroupa, P. 2003, MNRAS, 322, 231
Kuijken, K., & Tremaine, S. 1991, in Dynamics of Disk Galaxies, ed. B. Sundelius (Göteborg: Göteborg Univ. Press), 257
Kuijken, K., & Tremaine, S. 1994, ApJ, 421, 178
Kurucz, R. L. 1979, ApJS, 40, 1
Laney, C. D., Joner, M. D., & Pietrzyński, G. 2012, MNRAS, 419, L1637
Levine, E. S., Heiles, C., & Blitz, L. 2008, ApJ, 679, 1288
Luck, R. E., & Lambert, D. L. 2011, AJ, 142, 136
Majewski, S. R., Zasowski, G., & Nidever, D. L. 2011, ApJ, 739, 25
Marigo, P., Girardi, L., Bressan, A., et al. 2008, A&A, 482, 883
McWilliam, A., & Zoccali, M. 2010, ApJ, 724, 1491
Mészáros, Sz., Holtzman, J., García Pérez, A. E., et al. 2013, AJ, 146, 133
Miglio, A., Brogaard, K., Stello, D., et al. 2012, MNRAS, 419, 2077
Miglio, A., Chiappini, C., Morel, T., et al. 2013, MNRAS, 429, 423
Mosser, B., Barban, C., Montalbán, J., et al. 2011, A&A, 532, 86
Nataf, D. M., Udalski, A., Gould, A., Fouqué, P., & Stanek, K. Z. 2010, ApJL, 721, L28
Nidever, D. L., Zasowski, G., & Majewski, S. R. 2012, ApJL, 755, L25
Nordström, B., Mayor, M., Andersen, J., et al. 2004, A&A, 418, 989
Paczynski, B., & Stanek, K. Z. 1998, ApJL, 494, L219
Pietrinferni, A., Cassisi, S., Salaris, M., & Castelli, F. 2004, ApJ, 612, 168
Pietrinferni, A., Cassisi, S., Salaris, M., & Castelli, F. 2006, ApJ, 642, 797
Plez, B. 2012, Turbospectrum: Code for spectral synthesis, Astrophysics Source Code Library, record ascl:1205.004
Reimers, D. 1975, MSRSL, 6, 369
Rix, H.-W., & Bovy, J. 2013, A&ARv, 21, 61
Rix, H.-W., & Zaritsky, D. 1995, ApJ, 447, 82
Roeser, S., Demleitner, M., & Schilbach, E. 2010, AJ, 139, 2440
Roškar, R., Debattista, V. P., Quinn, T. R., & Wadsley, J. 2012, MNRAS, 426, 2089
Santiago, B. X., Brauer, D. E., Anders, F., et al. 2014, A&A, submitted
Schröder, K.-P., & Cuntz, M. 2005, ApJL, 630, L73
Scott, D. W. 1992, Multivariate Density Estimation: Theory, Practice, and Visualization (New York: Wiley)
Sellwood, J. A., & Binney, J. J. 2002, MNRAS, 336, 785
Siebert, A., Famaey, B., Minchev, I., et al. 2011, MNRAS, 412, 2026
Silverman, B. W. 1986, Density Estimation for Statistics and Data Analysis (London: Chapman and Hall)
Skrutskie, M. F., Cutri, R. M., Stiening, R., et al. 2006, AJ, 131, 1163
Sobeck, J., Majewski, S., Hearty, F., et al. 2014, in AAS Meeting Abstracts, 223, 440.06
Stanek, K. Z., & Garnavich, P. M. 1998, ApJL, 503, L131
Stanek, K. Z., Zaritsky, D., & Harris, J. 1998, ApJL, 500, L141
Steinmetz, M., Zwitter, T., Siebert, A., et al. 2006, AJ, 132, 1645
Stello, D., Huber, D., Bedding, T. R., et al. 2013, ApJL, 765, L41
Udalski, A., Szymanski, M., Kubiak, M., et al. 1998, AcA, 48, 1
Valentini, M., & Munari, U. 2010, A&A, 522, A79
Williams, M. E. K., Steinmetz, M., Binney, J., et al. 2013, MNRAS, 436, 101
Wilson, J. C., Hearty, F., Skrutskie, M. F., et al. 2010, Proc. SPIE, 7735, 46
Wright, E. L., Eisenhardt, P. R. M., Mainzer, A. K., et al. 2010, AJ, 140, 1868
Yong, D., Carney, B. W., & Friel, E. D. 2012, AJ, 144, 95
Zacharias, N., Finch, C. T., Girard, T. M., et al. 2013, AJ, 145, 44
Zasowski, G., Johnson, J. A., Frinchaboy, P. M., et al. 2013, AJ, 146, 81
Zasowski, G., Majewski, S. R., Indebetouw, R., et al. 2009, ApJ, 707, 510